Precessing spherical shells: flows, dissipation, dynamo and the lunar core

David Cébron, Raphaël Laguerre, Jerome Noir, Nathanaël Schaeffer

Precessing spherical shells: flows, dissipation, dynamo and the lunar core

D. Cébron[1]*, R. Laguerre[2], J. Noir[3], N. Schaeffer[1]

[1] Université Grenoble Alpes, CNRS, ISTerre, Grenoble, France

[2] Royal Observatory of Belgium, Brussels, Belgium

[3] Institute of Geophysics, ETH Zurich, Zurich, Switzerland

September 13, 2018

Abstract

Precession of planets or moons affects internal liquid layers by driving flows, instabilities and possibly dynamos. The energy dissipated by these phenomena can influence orbital parameters such as the planet's spin rate. However, there is no systematic study of these flows in the spherical shell geometry relevant for planets, turning any extrapolation to celestial bodies to pure speculation.

We have run more than 900 simulations of fluid spherical shells affected by precession, to systematically study basic flows, instabilities, turbulence, and magnetic field generation. We observe no significant effects of the inner core on the onset of the instabilities. We obtain an analytical estimate of the viscous dissipation. We propose theoretical onsets for hydrodynamic instabilities.

We extend previous precession dynamo studies towards lower viscosities, at the limits of today's computers. In the low viscosity regime, precession dynamos rely on the presence of large-scale vortices, and the surface magnetic fields are dominated by small scales. Interestingly, intermittent and self-killing dynamos are observed. Our results suggest that large-scale planetary magnetic fields are unlikely to be produced by a precessing dynamo in a spherical core. But this question remains open as planetary cores are not exactly spherical. Moreover, the fully turbulent dissipation regime has barely been reached.

Finally, we apply our results to the Moon, showing that turbulence can be expected in its liquid core during its whole history. Using recent experimental results, we propose updated formulas predicting the precession driven flow and dissipation in both the laminar and the turbulent regimes.

1 Introduction

The origin of the magnetic fields of planets and stars is attributed to the dynamo mechanism. It is commonly thought that most of the dynamos are powered by compositional and thermal convection in the liquid part of these objects. Nevertheless, this scenario is sometimes difficult to apply. This is for instance the case for the early Moon, for which the

*david.cebron@univ-grenoble-alpes.fr

intensity of the magnetic field generated by convection might not be sufficient (Stegman et al., 2003) or the Earth, where recent estimates of thermal and electrical conductivity of liquid iron imply that convection would be far less efficient than previously thought (Pozzo et al., 2012). Mechanical forcings constitute then alternative ways to sustain dynamo action (Le Bars et al., 2015), as shown numerically for libration (Wu and Roberts, 2013), tides (Cébron and Hollerbach, 2014; Vidal et al., 2018) or precession. The present study focuses on precession, which has already been demonstrated numerically to be able to grow a magnetic field in spherical shells (Tilgner, 2005, 2007), full spheres (Lin et al., 2016), cylinders (Nore et al., 2011; Giesecke et al., 2018) and cubes (Goepfert and Tilgner, 2016, 2018). Hence, the possibility of a precession driven dynamo in the liquid core of the Earth (Kerswell, 1996) or the Moon (Dwyer et al., 2011) cannot be excluded. However, current numerical simulations operate at viscosities many orders of magnitude higher than natural dynamos. The present work aims at shedding some light on the consequences of precession in spheres, including dissipation and magnetic field generation. To this end, we make extensive use of numerical simulations pushing down the viscosity to the limits of current supercomputers.

A rotating solid object is said to precess when its rotation axis itself rotates about a secondary axis that is fixed in an inertial frame of reference. The first theoretical studies of precession considered an inviscid fluid (Hough, 1895; Sloudsky, 1895; Poincaré, 1910). Assuming a uniform vorticity, they obtained a solution for the spheroid, called Poincaré flow, given by the sum of a solid body rotation and a potential flow. However, the Poincaré solution is modified by the existence of boundary layers, and some strong internal shear layers are also created in the bulk of the flow (Stewartson and Roberts, 1963). In 1968, Busse has taken into account these viscous effects as a correction to the inviscid flow in a spheroid, by considering carefully the Ekman layer and its critical regions (Busse, 1968; Zhang et al., 2010). Based on these works, Cébron et al. (2010) and Noir and Cébron (2013) have proposed models for the flow forced in precessing triaxial ellipsoids. Note that, beyond this correction approach, the complete viscous solution (including the fine description of all viscous layers) has been obtained in the two limit cases of a weakly (Kida, 2011) and strongly (Kida, 2018) precessing spherical container.

When the precession forcing is large enough compared to viscous effects, instabilities can occur in precessing spherical containers, destabilizing the Poincaré flow (e.g. Hollerbach et al. (2013)). First, the Ekman layers can be destabilized (Lorenzani, 2001) through standard Ekman layer instabilities (Lingwood, 1997; Faller, 1991). In this case, the instability remains localized near the boundaries. Second, the whole Poincaré flow can be destabilized, leading to a volume turbulence : this is the precessional instability (Malkus, 1968). It has been argued by Lorenzani (2001), and more recently by Lin et al. (2015), that the conical shears spawned at the critical latitudes can couple non-linearly with pairs of inertial modes, leading to the Conical Shear Instability (CSI) of Lin et al. (2015).

In this work, we will study the influence of the presence of a solid inner core on the precessional instability. We thus consider a spinning and precessing spherical shell filled with a conducting fluid. Adopting the approach used for ellipsoids by Noir and Cébron (2013), we obtain an explicit expression of the fluid rotation vector in the presence of an inner core. We then derive hydrodynamical stability criteria for the CSI involving conical shear layers spawned by the outer and the inner spherical shell. Finally, based on our hydrodynamic simulations, we investigate precession driven dynamos in different flow regimes. The pioneering results obtained by Tilgner (2005) are extended to smaller viscosities, in the hope to reach an asymptotic regime relevant for planetary fluid layers.

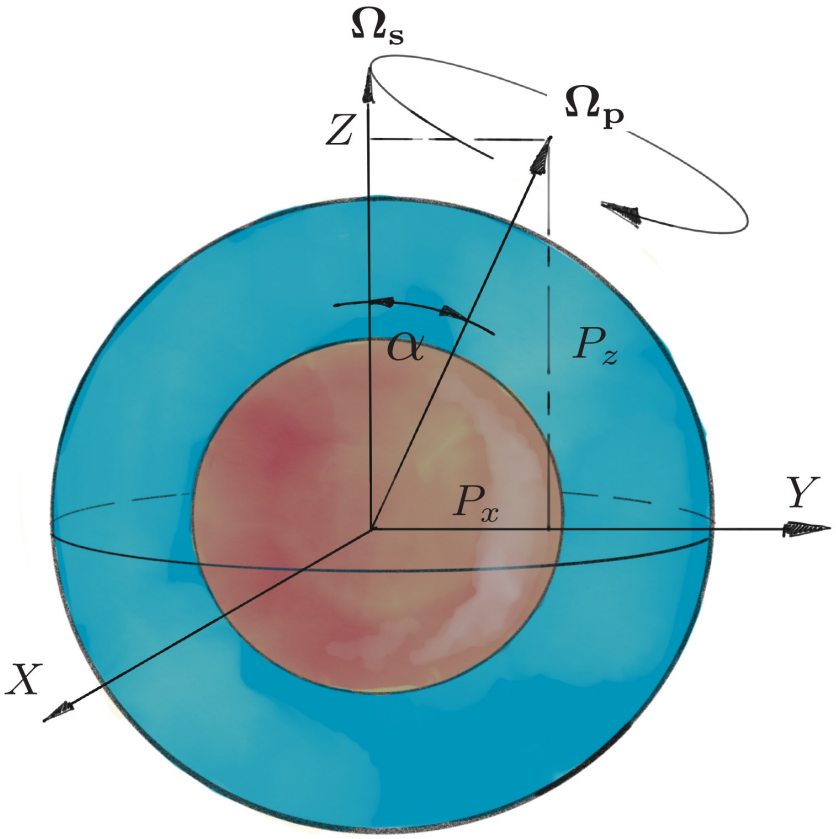

Figure 1: Schematic description of the problem.

Our paper is organized as follow. Section 2 presents the governing equations of the problem and a brief description of the numerical method used to solve the equations. A reduced model for the base flow in spherical shells is then derived and compared to numerical simulations in Section 3.1, while transition to unstable flows is studied in Section 3.2. Precession driven dynamos are studied in Section 4. Finally, we apply our findings to the Moon (§5) and draw some conclusions (§6).

2 Description of the problem and mathematical background

We consider an incompressible Newtonian fluid of density ρ, kinematic viscosity ν, electrical conductivity γ, and magnetic permeability μ, enclosed in a spherical shell of outer radius R and inner radius R_i. In the following, the outer boundary is also named CMB, for core-mantle boundary, whereas the inner one is also called ICB, for inner core boundary. The cavity rotates with an angular velocity $\mathbf{\Omega_s} = \Omega_s \hat{\boldsymbol{z}}$ and precesses along $\hat{\boldsymbol{k}}$ at Ω_p, with $\hat{\boldsymbol{k}} \cdot \hat{\boldsymbol{z}} = \cos\alpha$. We define the frame of precession as the frame of reference precessing at Ω_p, in which we construct a Cartesian coordinate $(\hat{\boldsymbol{x}}, \hat{\boldsymbol{y}}, \hat{\boldsymbol{z}})$ system centered on the sphere, with $\hat{\boldsymbol{z}}$ along $\mathbf{\Omega_s}$, $\hat{\boldsymbol{x}}$ such that $\mathbf{\Omega_p}$ is in the plane xOz and $\hat{\boldsymbol{y}} = \hat{\boldsymbol{z}} \times \hat{\boldsymbol{x}}$ (Fig. 1).

2.1 Mathematical formulation

Defining $\Omega_o = \Omega_s + \Omega_p$, we choose Ω_o^{-1} as the unit of time such that it remains relevant in both limits of large Ω_s or large Ω_p (see also Goepfert and Tilgner, 2016). We choose R and $R\Omega_o\sqrt{\mu\rho}$ as the respective units of length and magnetic field. In the frame of reference precessing at $\boldsymbol{\Omega}_p$ the dimensionless equations take the form:

$$\frac{\partial \boldsymbol{u}}{\partial t} + \boldsymbol{u}\cdot\nabla\boldsymbol{u} = -\nabla p + E\,\nabla^2\boldsymbol{u} - 2\frac{Po}{1+Po}\,\hat{\boldsymbol{k}}_p \times \boldsymbol{u} + (\nabla\times\mathbf{B})\times\mathbf{B}, \quad (1)$$

$$\nabla\cdot\boldsymbol{u} = 0 \quad (2)$$

$$\frac{\partial \mathbf{B}}{\partial t} = \frac{E}{Pm}\,\nabla^2\mathbf{B} + \nabla\times(\mathbf{u}\times\mathbf{B}), \quad (3)$$

$$\nabla\cdot\mathbf{B} = 0, \quad (4)$$

where p is the reduced pressure accounting for centrifugal forces. The four dimensionless parameters controlling the dynamics of the system are the Ekman, magnetic Prandtl, Poincaré numbers and aspect ratio, respectively defined by $E = \nu/(\Omega_o R^2)$, $Pm = \mu\gamma\nu$, $Po = \Omega_p/\Omega_s$, and $\eta = \frac{R_i}{R}$.

Note that with our choice of time scale, the rotation vector of the spherical container is $\tilde{\boldsymbol{\Omega}}_{\boldsymbol{s}} = (1+Po)^{-1}\hat{\boldsymbol{z}}$. Hence, our modified Ekman number is related to the more classical definition based on Ω_s, $E' = \nu/(\Omega_s R^2)$, as $E' = E(1+Po)$.

We also define spherical system coordinate (r,θ,ϕ), r being the radial distance, θ the colatitude, and ϕ the azimuthal angle (with Ox the axis of zero longitude).

2.2 Numerical approach

We impose no-slip boundary conditions at both boundaries, insulating boundary conditions for the magnetic field at the CMB and an inner core electrical conductivity equal to that of the fluid. The problem is solved using the XSHELLS code (freely available at `https://bitbucket.org/nschaeff/xshells`). This high performance, parallel Navier-Stokes solver works in spherical coordinates using a toroidal-poloidal decomposition and a pseudo-spectral approach. Note that with this approach, equations (2) and (4) are automatically satisfied. The spherical harmonic transforms are performed using the efficient SHTns library (Schaeffer, 2013) while the radial direction is discretized with finite differences. XSHELLS has been benchmarked on convective dynamo problems with or without a solid inner-core (Marti et al., 2014; Matsui et al., 2016). In the following, the so-called hydrodynamic simulations do not take into account the magnetic field ($\mathbf{B}$), whereas our so-called magnetohydrodynamic (MHD) simulations solve the full system (1)-(4). The range of hydrodynamic parameters investigated in this study are summarized in Fig. 2 and compared to the typical values expected for planetary cores. In addition we explore the range $0.2 < Pm < 20$ in our MHD simulations.

3 Hydrodynamics

3.1 Laminar Base Flow

The primary flow forced by precession in a sphere is mainly a tilted solid body rotation, a flow of uniform vorticity (Poincaré, 1910). In a spherical container, the direction and

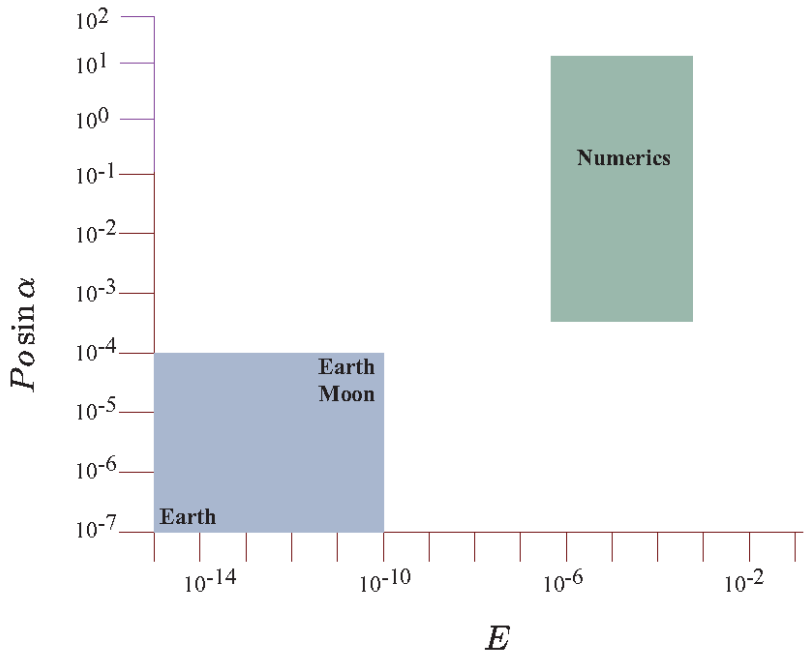

Figure 2: Parameter space covered by numerical studies and for typical planetary cores.

amplitude of the fluid rotation vector are governed by a balance between the viscous torque at the core-mantle boundary and the gyroscopic torque resulting from the precession of the liquid core (Busse, 1968; Noir et al., 2003). We briefly recall in section A.1 of appendix A the derivation of Busse (1968). A limitation of this general formulation, accounting for the Ekman boundary layer action, arises from the implicit nature of the final equation. Indeed, while approximate expressions can be obtained in certain limits (e.g. Boisson et al. (2012)), we cannot derive a general analytical explicit solution. In the context of a precessing ellipsoid, Noir and Cébron (2013) proposed an alternative to the torque balance, using a simpler ad-hoc viscous term. Using this successful approach in a spherical shell, we obtain an explicit expression of the dimensionless fluid rotation vector $\mathbf{\Omega}$ in the frame of precession (see section A.2 of appendix A for details):

$$\Omega_x = \frac{1}{1+Po}\frac{[\lambda_i+\chi\cos\alpha]\,\chi\sin\alpha}{\chi(\chi+2\lambda_i\cos\alpha)+|\underline{\lambda}|^2}, \tag{5}$$

$$\Omega_y = -\frac{1}{1+Po}\frac{\chi\lambda_r\sin(\alpha)}{\chi(\chi+2\lambda_i\cos\alpha)+|\underline{\lambda}|^2}, \tag{6}$$

$$\Omega_z = \frac{1}{1+Po}\frac{\chi(\chi\cos^2\alpha+2\lambda_i\cos\alpha)+|\underline{\lambda}|^2}{\chi(\chi+2\lambda_i\cos\alpha)+|\underline{\lambda}|^2}, \tag{7}$$

where $\chi = Po/\sqrt{E}$. Note that, in the sphere, there is always a single solution for the basic flow $\mathbf{\Omega}$, whereas multiple solutions can be obtained in spheroids or ellipsoids (Noir et al., 2003; Cébron, 2015; Vormann and Hansen, 2018).

In equations (5)-(7), the complex viscous damping coefficient $\underline{\lambda} = \lambda_r + \mathrm{i}\lambda_i$ of the spin-over mode is the sum of the (real) viscous damping λ_r and the (real) viscous correction to the inviscid frequency λ_i of the spin-over mode (35), such that $|\underline{\lambda}|^2 = \lambda_r^2 + \lambda_i^2$. For a full sphere, Greenspan et al. (1968) derived an expression for $\underline{\lambda}$ at the order $\mathcal{O}(\sqrt{E})$. To

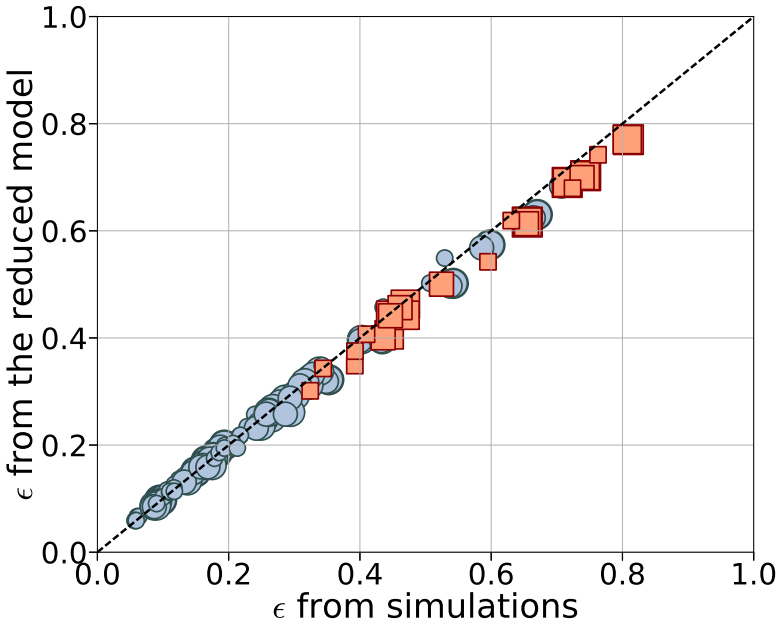

Figure 3: Comparison between the differential rotation ϵ of the simulations and the one of the reduced model. Blue circles and red squares represent stable and unstable flows, respectively.

account for the presence of an inner core, one can use

$$\underline{\lambda} = \underline{\lambda}_{(\eta=0)} \frac{1+\eta^4}{1-\eta^5} \tag{8}$$

for a no-slip inner core (Rieutord, 2001). Moreover, viscous corrections of $\underline{\lambda}$ should be considered for finite values of E (see appendix A.1). In the following, we account for these various corrections by calculating $\underline{\lambda}$ using equation (36).

Following Lin et al. (2015), we note ϵ the differential rotation $\epsilon = ||\boldsymbol{\Omega} - \tilde{\boldsymbol{\Omega}}_{\boldsymbol{s}}||$ between the fluid and the cavity. From the approximated solution of uniform vorticity (5)-(7) we derive the following analytical expression

$$\epsilon = \left| \frac{\chi \sin\alpha}{1+Po} \right| \frac{1}{\sqrt{\chi(\chi + 2\lambda_i \cos\alpha) + |\underline{\lambda}|^2}}. \tag{9}$$

The equations and the forcing being centro-symmetric, we estimate the uniform vorticity from the symmetric energy E_s of the flow that superimposes on the rotation of the cavity,

$$E_s = 1/2 \cdot \int \boldsymbol{u_s}^2 \mathrm{d}V, \tag{10}$$

with $\boldsymbol{u_s} = 1/2 \cdot (\boldsymbol{u_m}(\boldsymbol{r}) - \boldsymbol{u_m}(-\boldsymbol{r}))$ and $\boldsymbol{u_m} = \boldsymbol{u} - \boldsymbol{\Omega}_s \times \boldsymbol{r}$, we calculate ϵ according to $\sqrt{2E_s/I_c}$, where $I_c = 8\pi/15 \cdot (1-\eta^5)$ is the moment of inertia (per unit of mass) of the spherical shell enclosing the fluid. Fig. 3 shows that equation (9) is in quantitative agreement with the uniform vorticity component deduced from the the energy in our hydrodynamic simulations, which validate both our reduced model and the estimated differential rotation in the numerics from the symmetric energy.

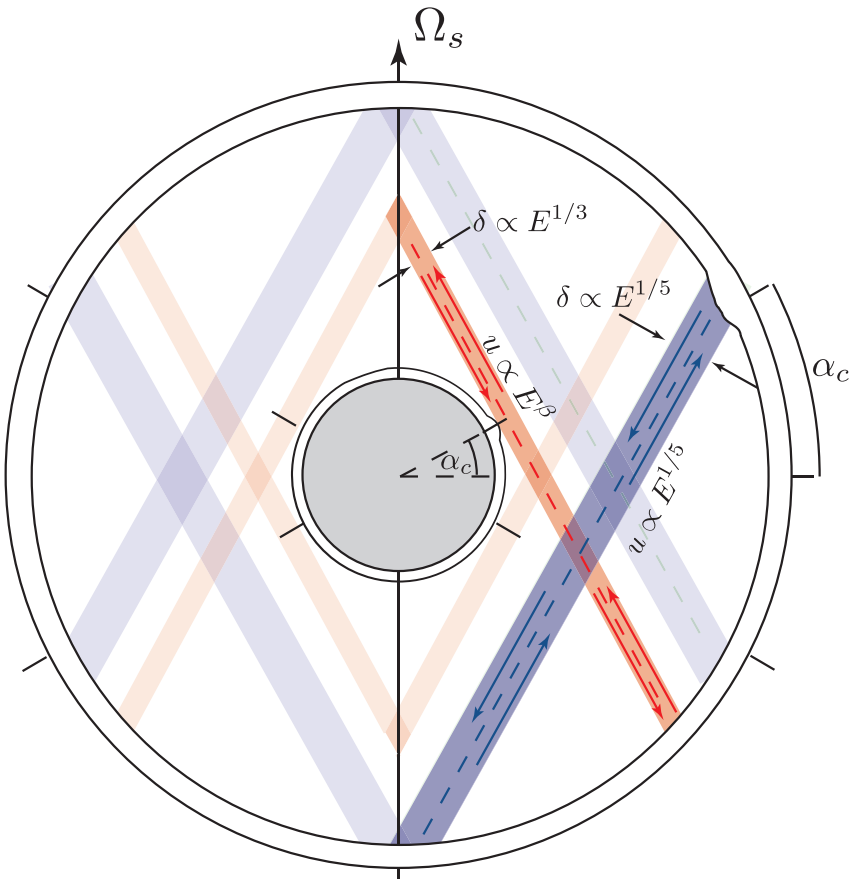

Figure 4: Schematic of the conical shear layers spawn from the critical latitude given by $\cos \alpha_c = 1/2$.

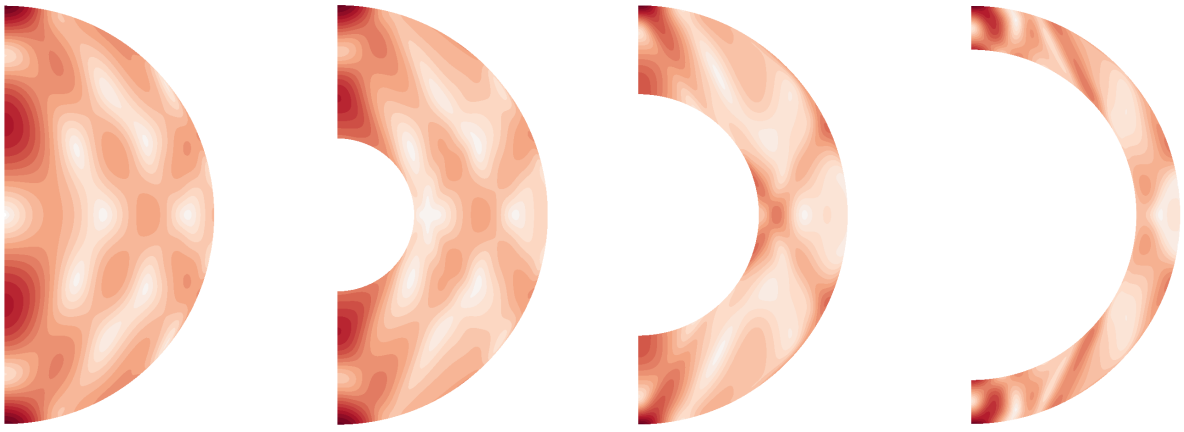

Figure 5: Contour plot of an instantaneous azimuthal average of the kinetic energy in the fluid frame for (a) $\eta = 0.01$, (b) $\eta = 0.3$, (c) $\eta = 0.5$ and (d) $\eta = 0.7$. In each case the flow is stable. $\alpha = 120°$, $Po = 1 \times 10^{-3}$ and $E = 3.0 \times 10^{-5}$. Contours range from 0 (white) to 0.028 (dark red)

.

In addition to the uniform vorticity flow, a secondary viscous circulation will develop in the interior due to the Ekman pumping at the ICB and at the CMB. In contrast with the classical uniform thickness of the planar Ekman boundary layer, oscillatory motions in a sphere result in local discontinuities at some critical latitudes, given by $\cos\alpha_c = \omega/2$, propagating in the interior along cones aligned with the axis of rotation (Fig. 4). For precession, $\omega = 1$, which corresponds to a critical latitude of 30° (Kerswell, 1995; Hollerbach and Kerswell, 1995; Stewartson and Roberts, 1963; Noir et al., 2001). Both the ICB and the CMB generate oblique shear layers. Kerswell (1995) proposed the following scalings for the width and strength of the flow in these oblique shear layers:

$$\delta_{CMB} \propto E^{1/5}, \qquad U_{CMB} \propto \epsilon E^{1/5}. \tag{11}$$

and,

$$\delta_{ICB} \propto E^{1/3}, \qquad U_{ICB} \propto \eta\epsilon E^{\beta}, \tag{12}$$

where β has been proposed to be either $\beta = 1/6$ (e.g. Kerswell, 1995; Calkins et al., 2010) or $\beta = 1/12$ (Le Dizès and Le Bars, 2017). The subscript refers to the region at the origin of the internal structures (Fig. 4).

To identify these structures in our numerical simulations, we look at the flow from a frame of reference attached to the mean rotation of the fluid. Fig. 5 represents the azimuthal average kinetic energy in a meridian plan for different inner core sizes, clearly exhibiting conical shear layers. The ones spawned from the ICB critical latitude being more intense, they quickly dominate as the inner core radius increases.

3.2 Hydrodynamic instabilities

We track the instability onset by looking for non-zero anti-symmetric energy (Lorenzani, 2001; Lin et al., 2015):

$$E_a = 1/2 \cdot \int \boldsymbol{u_a}^2 \mathrm{d}V, \tag{13}$$

where $\boldsymbol{u_a} = 1/2 \cdot (\boldsymbol{u(r)} + \boldsymbol{u(-r)})$. Although centro-symmetric unstable flows exist (Hollerbach et al., 2013), they are however limited to a narrow range of parameters with moderate to large values of E (Lin et al., 2015). Disregarding these possible instabilities, we focus on unstable flows which break the centro-symmetry, i.e. with $E_a \neq 0$.

It has been recently argued by Lin et al. (2015) and Lorenzani (2001) that the oscillating conical shear layers, originating from the CMB Ekman boundary layers, can couple non-linearly with two inertial modes, $\boldsymbol{u}_1$ and $\boldsymbol{u}_2$, leading to a parametric resonance, the so-called Conical Shear Instability (CSI, Lin et al., 2015). For precession, the two free inertial modes are subject to the following selective rules (Kerswell, 2002):

$$\begin{aligned} \omega_1 \pm \omega_2 &= 1, \\ m_1 \pm m_2 &= 1, \\ l_1 \pm l_2 &= 1. \end{aligned} \tag{14}$$

where $\omega_{1,2}$ and $m_{1,2}$ are the frequency and azimuthal wave numbers of the two free inertial modes, respectively. $l_{1,2}$ is the degree of the Legendre polynomial characterizing the latitudinal complexity.

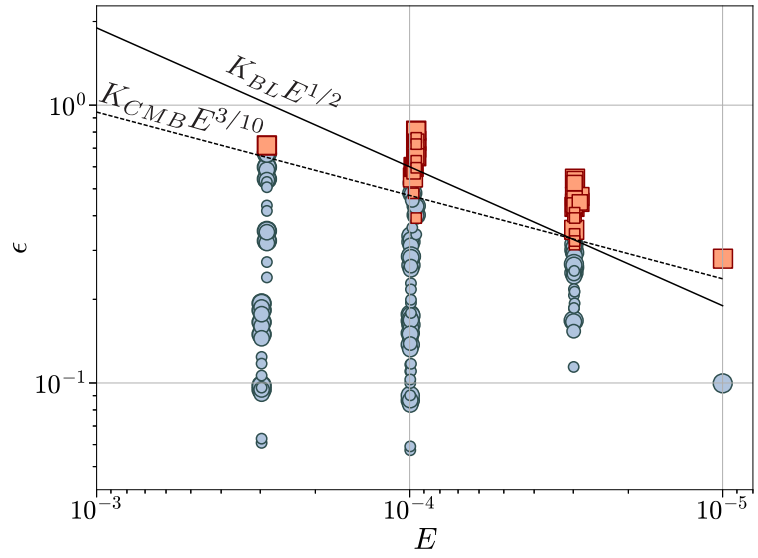

(a)

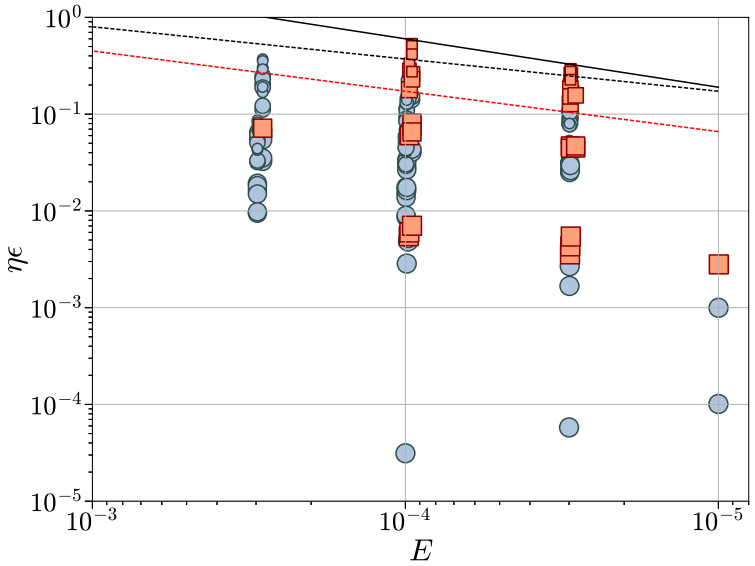

(b)

Figure 6: Stability criterion (a) for CMB related instabilities, the dashed and solid lines represents the theoretical CSI-CMB (equation 16 with $K_{CMB} = 8$) and BL-CMB (equation 18 with $K_{BL} = 60$), respectively. (b) for the ICB related instabilities, assuming $K_{ICB} = 8$ and $K_{BL} = 60$ in equations (17) and (19), with $\beta = 1/6$ and $\beta = 1/12$. In both figures, the blue circles and the red squares represent the stable and unstable flows respectively. The symbol sizes are inversely proportional to η.

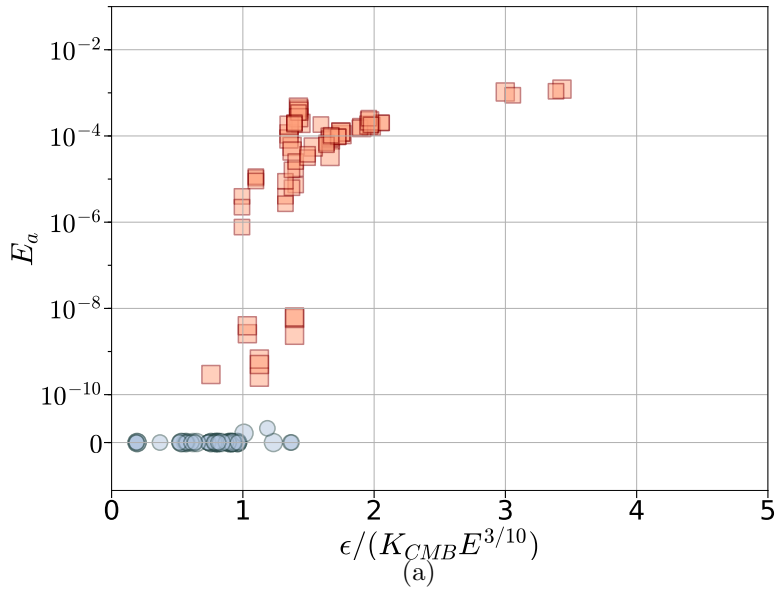

(a)

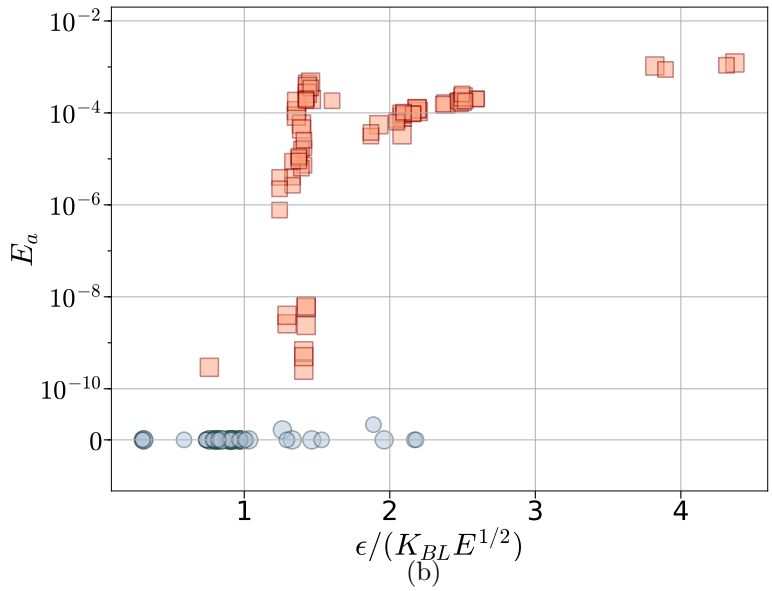

(b)

Figure 7: Anti-symmetric energy as a function of the criticality factor $\epsilon/(K_{CMB}E^{3/10})$ for the CSI-CMB (a) and $\epsilon/(K_{BL}E^{1/2})$ for the BL-CMB (b), with $E \leq 3 \times 10^{-5}$. In both figures, the blue circles and the red squares represent the stable and unstable flows respectively. The symbol sizes are inversely proportional to η.

(a) (b) (c)

Figure 8: Isosurfaces of the anti-symmetric energy in the mean fluid rotating frame frame for (a) $\eta = 0.01$, $Po = 8\times10^{-3}$ (b) $\eta = 0.3$, $Po = 8\times10^{-3}$ and (c) $\eta = 0.7$, $Po = 8.5\times10^{-3}$. In each case $\alpha = 120^\circ$ and $E = 3.0 \times 10^{-5}$. Color correspond to positive (black) and negative (white) axial velocity. The snapshots are taken during the initial growth phase of the instability.

Based on the scaling of the oblique shear layers emanating from the CMB (Fig. 4), Lin et al. (2015) proposed that the onset of the CSI is governed by a critical value of the differential rotation ϵ, scaling as

$$\epsilon_c \propto E^{3/10}, \tag{15}$$

in agreement with their numerical simulations in a full sphere as well as the experimental results from Goto et al. (2014). The same argument can be used in the spherical shell to derive a criteria for the onset of a CSI driven by the oblique shear layers emanating from the CMB as well as from the ICB.

For clarity, we name CSI-ICB and CSI-CMB, the parametric instabilities of the conical shear layers spawned from the Ekman boundary layer of the ICB and CMB, respectively. Adopting the same approach as Lin et al. (2015), with the scaling of shear layers shown in Fig. 4, we obtain

$$\epsilon_c = K_{CMB} E^{3/10}, \tag{16}$$

for the CSI-CMB and

$$\epsilon_c = K_{ICB} \frac{E^{1/2-\beta}}{\eta} \tag{17}$$

for the CSI-ICB, where K_{CMB}, K_{ICB} are two constants (β is introduced in equation 12).

In our data, we note that the two stability criteria are difficult to distinguish. In addition, the CMB and ICB Ekman boundary layers may be unstable to a local shear instability. The onset of this boundary-layer instability is characterized by the local Reynolds number $Re_{bl} = v\delta/\nu \approx 55$ (e.g. Lorenzani, 2001; Sous et al., 2013) based on the Ekman layer thickness $\delta = \sqrt{\nu/\Omega} = \sqrt{E}R$ and the maximum (differential) tangential velocity v at the edge of the boundary layers, with $v = \epsilon$ at the CMB and $v = \eta\epsilon$ at the ICB. The stability criteria for the ICB and CMB read

$$Re_{CMB} = \frac{\epsilon}{\sqrt{E}} > K_{BL}, \tag{18}$$

$$Re_{ICB} = \frac{\eta\epsilon}{\sqrt{E}} > K_{BL}, \tag{19}$$

with $K_{BL} \approx 55$ (Lorenzani, 2001; Sous et al., 2013), and the associated instabilities will be noted respectively BL-CMB and BL-ICB. In all cases, the outer boundary will become unstable first.

Following 3.2, we arbitrarily distinguish the stable and unstable cases by $E_a < 10^{-10}$ and $E_a > 10^{-10}$, respectively. To unravel the underlying destabilizing mechanism, we represent our results in an (ϵ, E) parameter space against the above mentioned onset criterion for the CSI-CMB (Fig. 6a) and $(\eta\epsilon, E)$ for their ICB counter part (Fig. 6b). We cover a wide range of parameters, $\eta = 0, 0.01, 0.1, 0.3, 0.35, 0.5, 0.7$, $Po < 0.1$ and $E < 3 \times 10^{-4}$. From Fig. 6b, we can clearly exclude both CSI-ICB and BL-ICB. Fig. 6a suggests that in our numerical simulations the first instability is a CSI-CMB at moderate to large Ekman numbers. Meanwhile, below $E = 3 \times 10^{-5}$, our theory predicts that the boundary layer is unstable before the CSI-CMB. To test this prediction, simulations at much lower Ekman numbers are required. This can be further illustrated by considering the anti-symmetric energy as a function of the two criticality factors, $\epsilon/E^{3/10}$ for the CSI-CMB and $\epsilon/E^{1/2}$ for the BL-CMB, for the simulations of fig. 6 with $E \leq 3 \times 10^{-5}$ (Fig. 7). A striking result in this study is the robustness of the instability criteria scaling for all inner core radii investigated up to $\eta = 0.7$. Meanwhile we note from Fig. 7 that the small inner core tends to become unstable at higher values of the critical parameter, which suggests that K_{BL} and K_{CMB} may depend on η.

In order to distinguish clearly between the two mechanisms one should carry out numerical simulations in the range $10^{-8} < E < 10^{-6}$, a range of values still hardly accessible. Further considerations regarding the prevalence of a possible viscous boundary layer at the ICB will be discussed in the last section in a geophysical context at very low Ekman numbers.

Independently of the true acting mechanism, Fig. 7 alos shows that energy stored in the instability quickly growth by more than three orders of magnitude as we slightly increase the criticality factor above onset. Further calculations at lower Ekman numbers would be necessary to uncover a saturation scaling law, which remains out of reach in our simulations.

3.3 Instability flow structure

Fig. 8 represents the axial velocity during the growth phase of the instability in the system for three different inner core sizes ($\eta = 0.01, 0.3, 0.7$) and for the following control parameters, $\alpha = 120°$, $E = 3.0 \times 10^{-5}$, $Po = 7 \times 10^{-3}$ except for the largest inner core for which the instability is detected only for $Po = 8.5 \times 10^{-3}$. Not surprisingly, the smallest inner core (Fig. 8a) is comparable to the full sphere case of Lin et al. (2015) with two inertial modes of wave numbers $m = 17$ and $m = 18$ developing in the outer part of the fluid domain. As we increase the volume of the inner core, the modes involved in the parametric resonance remains high order near onset (Fig. 8b and c) and tend to develop in regions above and below the inner core, again exhibiting pairs of inertial modes satisfying the parametric resonant conditions. These results near onset suggest that a CSI-CMB mechanism is operating at this low value of the Ekman number.

Fig. 9 shows the total anti-symmetric kinetic energy and the anti-symmetric kinetic energy for each azimuthal wave numbers m for increasing Poincaré numbers, from $Po = 7 \times 10^{-3}$ just above onset to about 2 times critical at $Po = 1.3 \times 10^{-2}$ for $\eta = 0.01$. Near onset, the parametric instability remains at a saturated state (Fig. 9(a)). As shown by Fig. 9(b), a very small increase of the forcing at $Po = 8.5 \times 10^{-3}$ leads to a quasi periodic

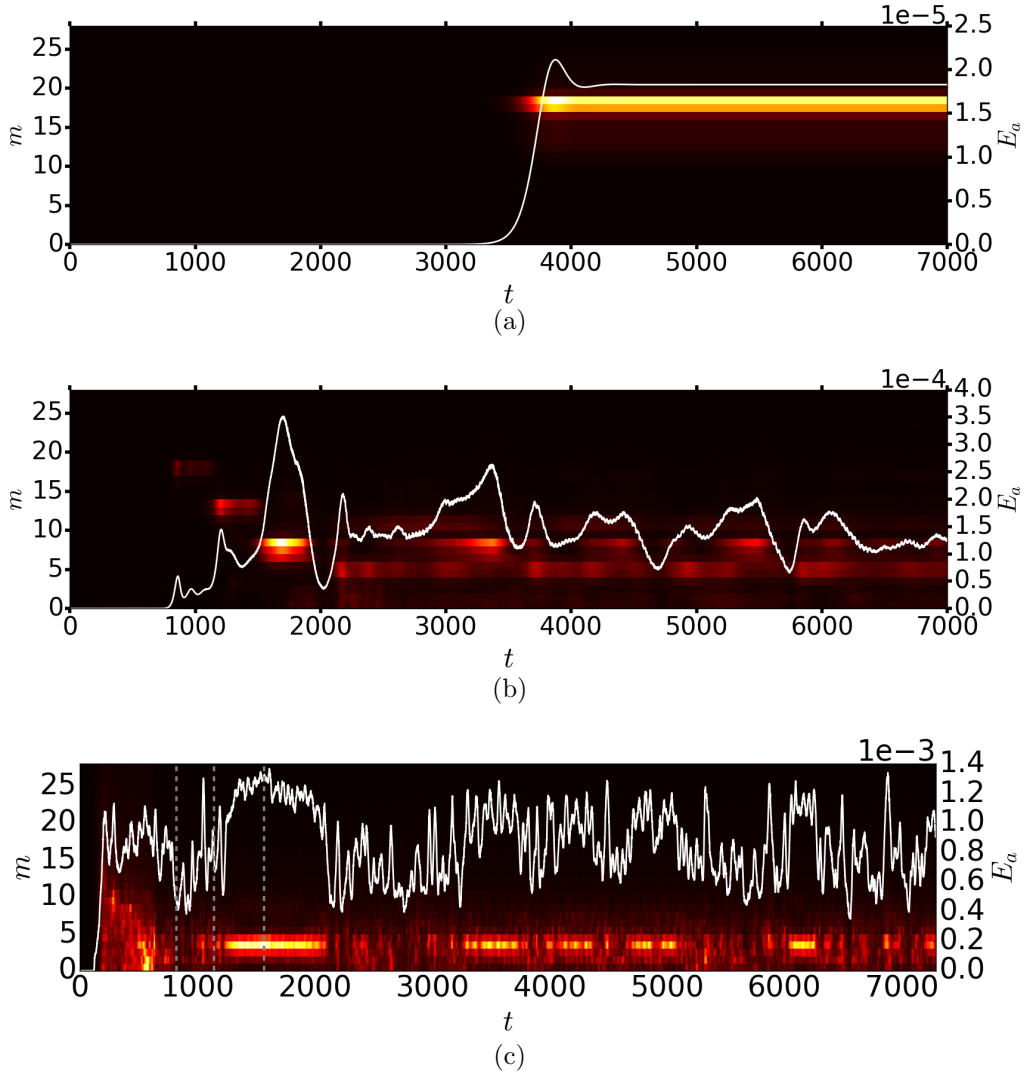

Figure 9: Time evolution of the anti-symmetric kinetic energy of each azimuthal mode m in the fluid frame (color map) and of the total anti-symmetric kinetic energy (White solid line). Fixed $\eta = 0.01$, $\alpha = 120°$ and $E = 3.0 \times 10^{-5}$. The Poincaré number increases from (a) $Po = 7 \times 10^{-3}$, (b) $Po = 8.5 \times 10^{-3}$ and (c) $Po = 1.3 \times 10^{-2}$, with dashed gray lines corresponding to the times of figure 10.

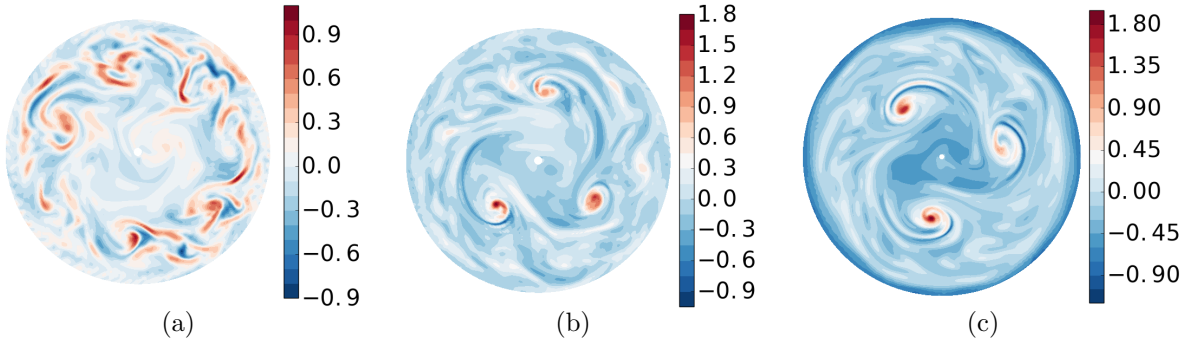

(a) (b) (c)

Figure 10: Snapshot of an equatorial cross-section of the axial vorticity ω_z in the fluid frame for $\eta = 0.01$, $Po = 1.3 \times 10^{-2}$, $\alpha = 120°$ and $E = 3.0 \times 10^{-5}$, same as Fig. 9. (a) $t = 822$, (b) $t = 1142$ and (c) $t = 1567$

behaviour of the system with a typical period of order $T = 500$. Despite the modest increase in Po, we observe an anti-symmetric energy at saturation that is an order of magnitude larger, yet pairs of modes in parametric resonance can be clearly identified supporting a CSI-CMB underlying mechanism.

In Fig. 9(c), we further increase the precession rate to $Po = 1.3 \times 10^{-2}$. We do not observe a clear initial growth of any particular modes but intermittent states with chaotic and quasi steady phases appear. At $Po = 1.3 \times 10^{-2}$ the dynamic of system is no longer quasi periodic in time, rapid fluctuations are observed together with periods of stable energy of modes with $m = 3$ as for instance between $t \sim 1250$ and $t \sim 2100$. The system alternates between phases in which E_a is concentrated in the $m = 3$ azimuthal mode, contrasting with phases during which E_a is distributed over a wider range of m. In Fig. 10, we show that 3 cyclonic LSV are seen in the phases where E_a is concentrated in $m = 3$, while they are absent in the other phases.

Finally, we increase η from 0.3 to 0.7 at $E = 3.0 \times 10^{-5}$, $Po = 8.5 \times 10^{-3}$, $Po = 1.3 \times 10^{-2}$ and $Po = 2 \times 10^{-2}$, to investigate the influence of the inner core on the dynamics above the onset. At $Po = 8.5 \times 10^{-3}$ we observe a similar dynamics as for $\eta = 0.01$ with quasi-periods increasing with η, the mode structures are qualitatively similar to the full sphere as seen on Fig. 8. While at $\eta = 0.1, 0.3$ we could still observe LSV, although with a shorter life time, they completely disappear for $\eta > 0.3$ for $Po = 1.3 \times 10^{-2}$ and $Po = 2 \times 10^{-2}$. At this Poincaré numbers with moderate to large inner cores, the flow exhibits small scale structures with rapid temporal variations. In contrast with the mode-coupling regime, the typical time scale of the energy fluctuations decreases with increasing inner core size. These calculations quickly become computationally challenging as the Poincaré number is increased. Since an extensive survey of the parameter space to characterise the onset of the LSV is beyond the scope of this paper, we did not explore the higher Po range where the LSV may be driven even in the presence of a large inner core.

3.4 Energy Dissipation

The total viscous dissipation

$$D_\nu = E \int (\nabla \times \boldsymbol{u})^2 \mathrm{d}V \tag{20}$$

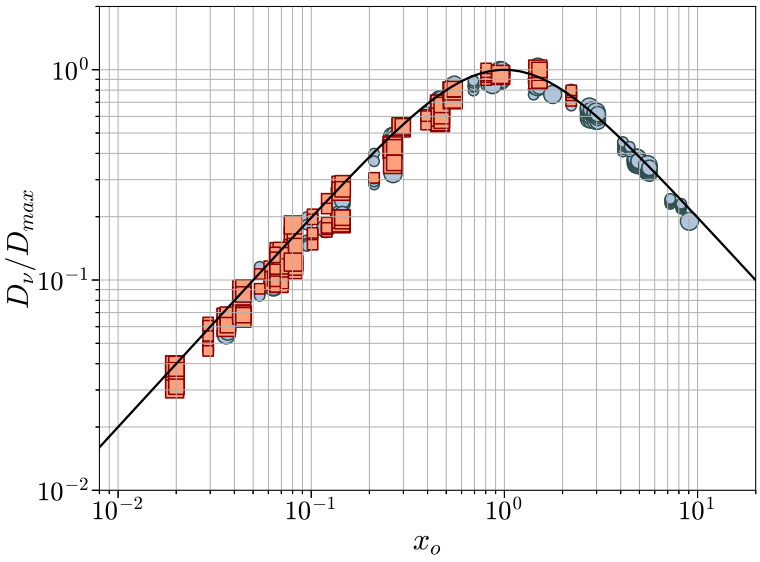

Figure 11: Viscous dissipation obtained in simulations (symbols) and predicted (solid line) by equation (25), showing the expected maximum $D_\nu/D_\nu^{max} = 1$ for $x_o = 1$. The blue circles and red squares represent dissipation for stable and unstable flows, respectively. The symbol sizes are inversely proportional to the inner core size η.

arises, in absence of instability, purely through viscous friction in the boundary layers at the inner and outer walls and in the oblique shear layers in the bulk.

First, we consider the oblique shear layers in the bulk. To calculate the associated dissipation, one can restrict the volume integral to the shear layers in equation (20). For the conical shear layer originating from the CMB, we obtain a dissipation in $\epsilon^2 E^{6/5}$ using the scalings (11), whereas for the one originating from the ICB, we find a dissipation in $\epsilon^2\eta^2 E$ using the scalings (12) with $\beta = 1/6$. For asymptotically small Ekman numbers $E \ll 1$, both contributions become negligible compared to the Ekman boundary layer dissipation. Thus, the total viscous dissipation D_ν reads $D_\nu = \mathbf{\Gamma}_\nu \cdot (\mathbf{\Omega} - \tilde{\mathbf{\Omega}}_{\boldsymbol{s}})$ where $\mathbf{\Gamma}_\nu$ is the associated viscous torque. Having shown in section 3.1 that the reduced model performs equally well than the model of Busse (1968) but provides explicit expression for ϵ, we use equation (41) for $\mathbf{\Gamma}_\nu$. The dissipation is then

$$D_\nu = -I_c\,\epsilon^2\,\lambda_r\,\sqrt{E}, \tag{21}$$

which only differs by a factor $\Omega^{1/2}$ from the one obtained with the viscous torque (40) of the Busse (1968) model. Replacing finally ϵ with equation (9), equation (21) becomes

$$D_\nu = \frac{8\pi(1-\eta^5)|\lambda_r|\,\sqrt{E}}{15|1+Po|^2}\,\frac{|\chi\sin\alpha|^2}{|\chi(\chi+2\lambda_i\cos\alpha)+\lambda_r^2+\lambda_i^2|}. \tag{22}$$

Note that equation (22) predicts that D_ν is maximized over E for $E = Po^2/|\underline{\lambda}|^2$. Indeed, $D_\nu \propto \epsilon^2\sqrt{E}$, and equation (9) shows that ϵ is rather constant for $|\underline{\lambda}|E^{1/2} < Po$ but decreases as $E^{-1/2}$ for $|\underline{\lambda}|E^{1/2} > Po$. Defining $x_o = |\underline{\lambda}|E^{1/2}/Po$, maximum dissipation can be thus expected around $x_o = 1$.

To compare the theory with the simulations, we rewrite equation (22) as

$$D_\nu = \frac{2x_o}{1+\gamma x_o + x_o^2} D_{max}, \tag{23}$$

with $x_o = |\underline{\lambda}|E^{1/2}/Po$, $\gamma = 2\lambda_i \cos\alpha/|\underline{\lambda}|$ and where

$$D_{max} = \frac{4\pi}{15} \frac{(1-\eta^5)|\lambda_r| Po \sin^2\alpha}{(1+Po)^2|\underline{\lambda}|} \tag{24}$$

is the maximum viscous dissipation when E is varied. Showing the evolution of D_ν/D_{max} in Fig. 11, the dissipation, for purely stable flows, collapses rather well on the following approximation of equation (23),

$$D_\nu = \frac{2x_o}{1+x_o^2} D_{max}, \tag{25}$$

obtained by neglecting λ_i in equation (23). As expected from equation (25), the maximum viscous dissipation $D_\nu = D_{max}$ is reached in our simulations for $x_o = 1$. Note that, considering Fig. 11, the current Earth would be at $x_0 \sim 1$, i.e. near the maximum of dissipation, whereas the current Moon would be at $x_o \sim 10^{-3}$. It is interesting to note that D_{max} is independent of E, thus of the viscosity, providing a robust upper bound for precession driven dissipation in spherical shells.

Maybe more surprisingly, Fig. 11 shows that, even when the interior flow is unstable, the results are still in agreement with equation (22). It implies that, in the range of accessible parameters, the dissipation is dominated by the laminar dissipation in the boundary layers. Actually, according to the experiments of Sous et al. (2013), the influence of turbulence becomes significant when the local Reynolds number $Re = \epsilon/E^{1/2}$ is larger than ~ 150. Only 4 simulations are in this range (with however $Re < 250$), which does not allow to check this expected change of behavior.

4 Precession driven dynamos

We now add a magnetic field and solve the whole system of equations (1)-(4). In all our simulations, the initial magnetic and velocity fields are random. We have produced two databases totaling more than 900 simulations. The first set of more than 750 simulations consists in a broad search in the 4-dimensional parameter space (E, η, Po, Pm) which resulted in only few dynamos. In this set, when an inner-core is present it is conducting with the same conductivity as the fluid. The non-dynamo runs of this set were extensively used in the previous sections. The second set of runs uses an insulating inner-core and is focused on several 1-dimensional paths across the parameter space, yielding a few tens of self-sustained dynamos. The explored parameters are summarized in figure 12, and the full databases are made freely available at `https://doi.org/10.6084/m9.figshare.7017137`.

4.1 Beyond Tilgner (2005)

Tilgner (2005) has shown that precessing spheres can generate dynamos, either driven by the Ekman pumping of the forced basic laminar flow (at relatively large values of E),

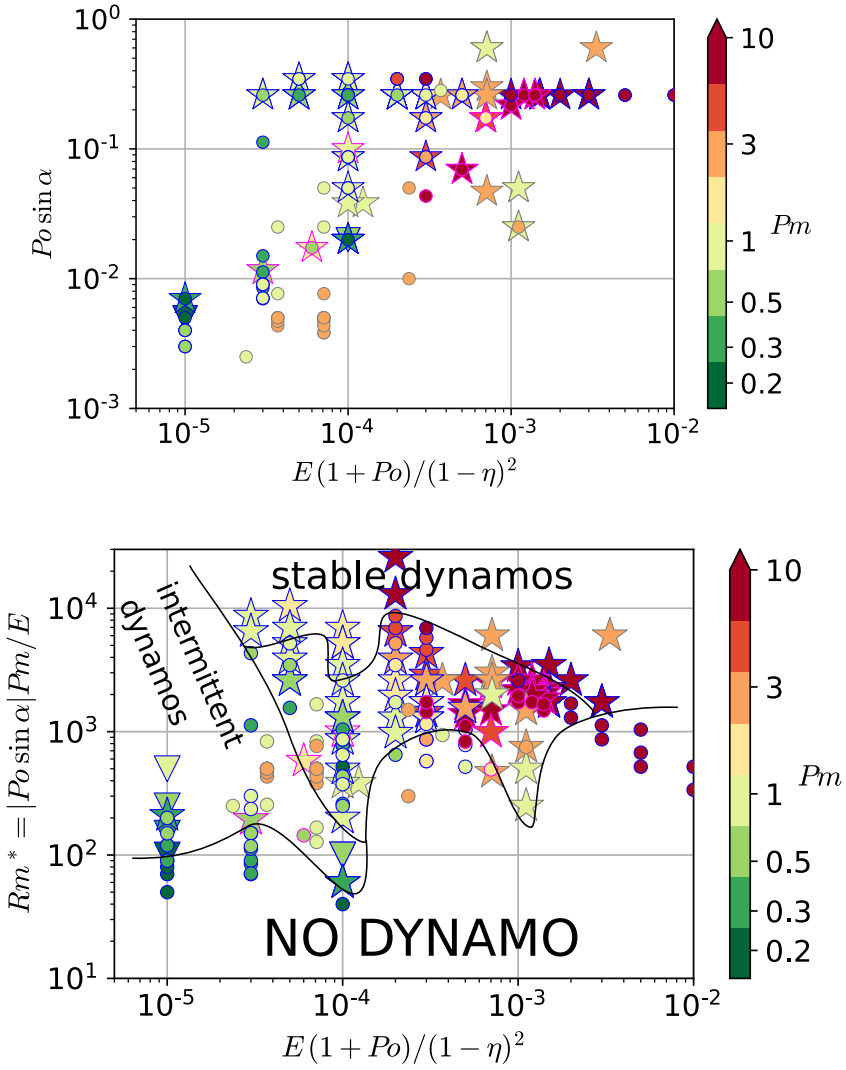

Figure 12: Saturated dynamos (stars), self-killing dynamos (triangles) and non-dynamo (circles) represented in two parameter-space planes. Symbols outlined in pink are from Lin et al. (2016); a grey outline indicates a conducting inner-core; a blue outline stands for a small insulating inner-core ($\eta = 0.1$) or no inner-core (full sphere). The x-axis is the standard Ekman number based on the gap width.

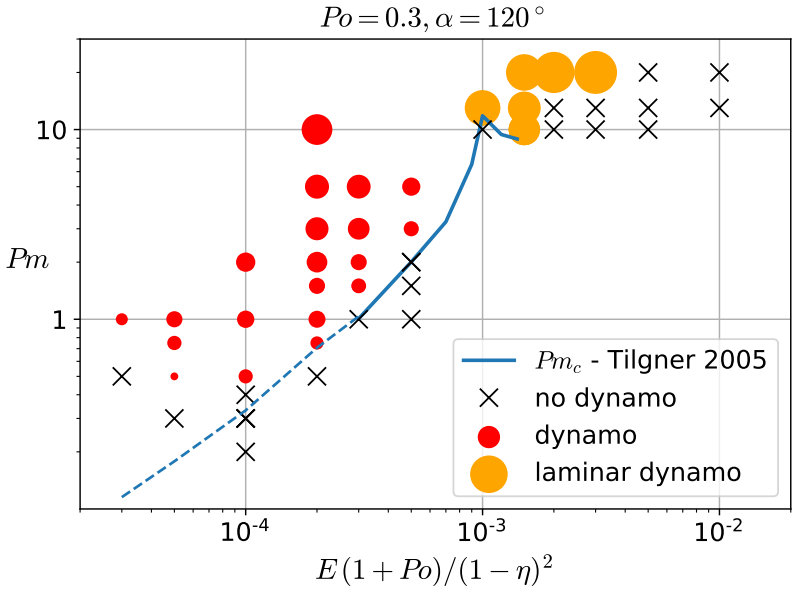

Figure 13: Successful dynamo (circle) and non-dynamo (cross) simulations for the precession parameters of Tilgner (2005): $\eta = 0.1$, $Po = 0.3$, $\alpha = 120°$, with a stress-free insulating inner core. The solid blue line is the critical Pm for dynamo action found by Tilgner (2005), and the dashed blue line is the law $Pm_c = 300 E_a^{-1/2} E\,(1+Po)/(1-\eta)^2$ that he proposed (cast to our definition of E). The area of the dots is proportional to the magnetic energy.

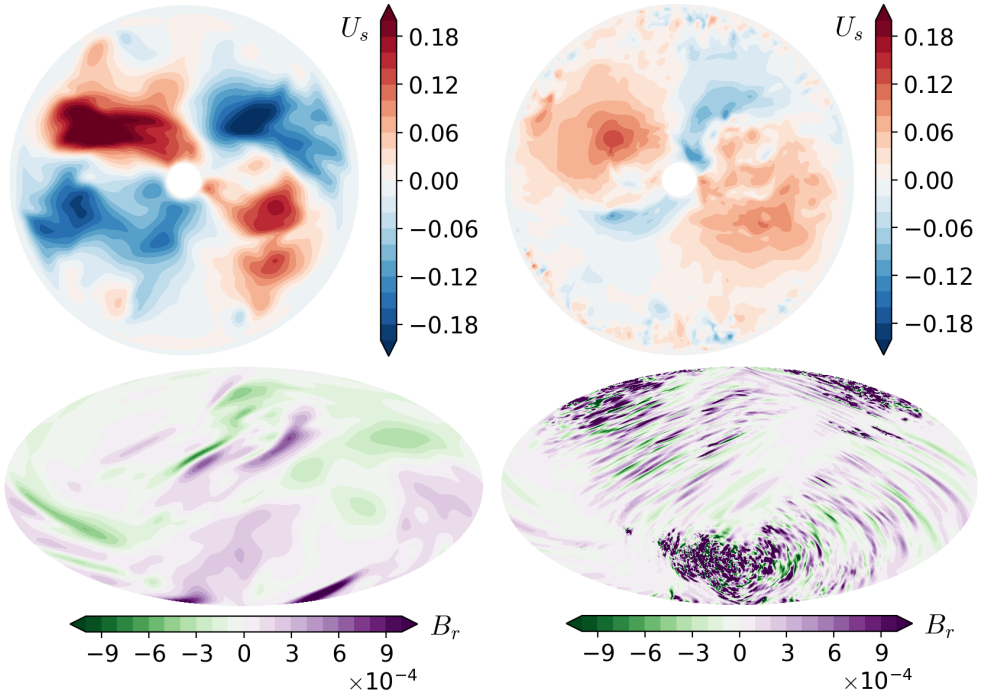

Figure 14: Radial velocity in the equatorial plane (top) and radial magnetic field at the core surface (bottom) for two different values of the viscosity, near the onset of dynamo action. Lower viscosity (right: $E = 1.87 \times 10^{-5}$, $Pm = 1$) results in much smaller scales in both velocity and magnetic fields than the larger viscosity (left: $E = 1.25 \times 10^{-4}$, $Pm = 0.75$). Both cases have $Po = 0.3$, $\alpha = 120°$ and a small insulating inner-core ($\eta = 0.1$)

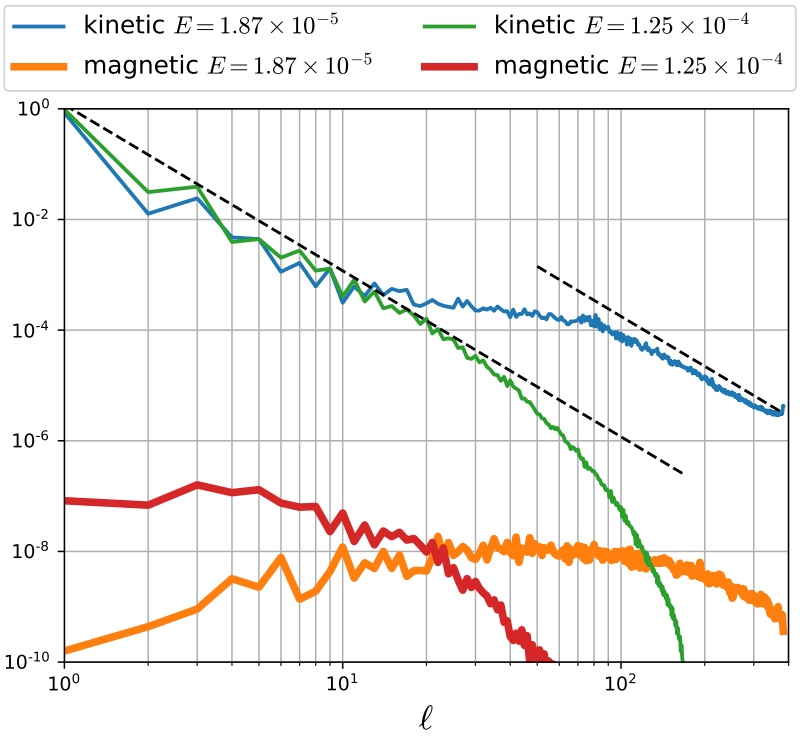

Figure 15: Magnetic and kinetic energy spectra as a function of spherical harmonic degree ℓ at the fluid surface for the magnetic field and below the Ekman layer for the velocity field. The black dashed lines indicate slopes of -3 for the kinetic energy spectra. The two cases have $Po = 0.3$, $\alpha = 120°$, a small insulating inner-core ($\eta = 0.1$) and $Pm = 1$ and differ by their Ekman number $E = 1.25 \times 10^{-4}$ and $E = 1.87 \times 10^{-5}$, the latter displaying more energy at smaller scales.

or driven by the anti-symmetric flow associated with instabilities (at smaller E). More recently, Lin et al. (2016) found that large scale vortices are sometimes generated by these instabilities, and that they contribute to magnetic field generation.

We first focus on the precession rate $Po = 0.3$ and precession angle $\alpha = 120°$ for which the onset for dynamo action has been determined by Tilgner (2005) in his figure 4. Our results are summarized in figure 13, showing that our non-linear dynamos are correctly separated by his critical magnetic Prandtl number Pm_c curve (the solid line in figure 13). Thanks to today's computing facilities and to the highly efficient XSHELLS code, we were able to further decrease the viscosity by a factor 10. Since the forcing ($Po = 0.3$) is kept constant here, this leads to turbulent flows, which require high resolutions and a high degree of parallelization to simulate. At large and small Ekman numbers, we observe the apparition of two local minima for the critical magnetic Prandtl number Pm_c of the dynamo onset: one for $E \simeq 1.5 \times 10^{-3}$ and one for $E \simeq 10^{-4}$. If the former can be explained by the transition from base flow driven dynamos to instability driven dynamos, the latter is more difficult to interpret. Indeed, Tilgner (2005) explains the decrease of the critical magnetic Prandtl number Pm_c in the range $10^{-4} \leq E \leq 10^{-3}$ by assuming that dynamo action takes place above a critical magnetic Reynolds number $Rm_c \propto E_a^{1/2} Pm_c/E$ based on the anti-symmetric energy E_a. For $E \leq 10^{-4}$, this law is no longer valid as turbulent fluctuations seem to have a negative effect on dynamo action, both in terms of onset (Pm_c increases when decreasing E) and field intensity (as shown by the diminishing circle area in figure 13). What happens when lowering the viscosity is illustrated in figures 14 and 15. Although the large scale flow presents similar strength and shape at $E = 2 \times 10^{-4}$ and at $E = 3 \times 10^{-5}$, small-scale instabilities develop near the outer shell in the latter case. This results in a shredding of the surface magnetic field to small scales. In figure 15, comparing $E = 3 \times 10^{-5}$ to $E = 2 \times 10^{-4}$, the large scale magnetic field is reduced by a factor 100, while the magnetic energy peaks at scales that will be strongly attenuated with distance, and likely to be undetectable at the planet's surface.

However, this path with fixed $Po = 0.3$ does not lead to planets, for which $Po \ll 1$, and we now vary the precession rate.

4.2 Varying the precession rate

Surprisingly, when setting $Po = 0.2$ or $Po = 0.4$ instead of $Po = 0.3$, the critical magnetic Prandtl number Pm_c required for dynamo action increases (see Fig. 12a). This means that the flow generated by a precession rate $Po = 0.2$ or $Po = 0.4$ is less efficient than the one obtained at precession rate $Po = 0.3$. This already highlights the complicated landscape in which we are trying to find dynamos. Specific values of the precession rate will lead to dynamos whereas neighboring values will not. This is apparent in figure 12, where circles (decaying magnetic field) and stars (dynamos) are entangled. We have not been able to find simple parameter combinations that allowed to disentangle them. For instance, we introduce a precession-based magnetic Reynolds number $Rm^* = |Po \sin \alpha| Pm/E$. Figure 12b shows that a stable dynamo is found for a low $Rm^* = 60$ (at $E = 10^{-4}$, $Po = 0.02$, $Pm = 0.3$), while several cases at $Rm^* \geq 4000$ do not produce a magnetic field.

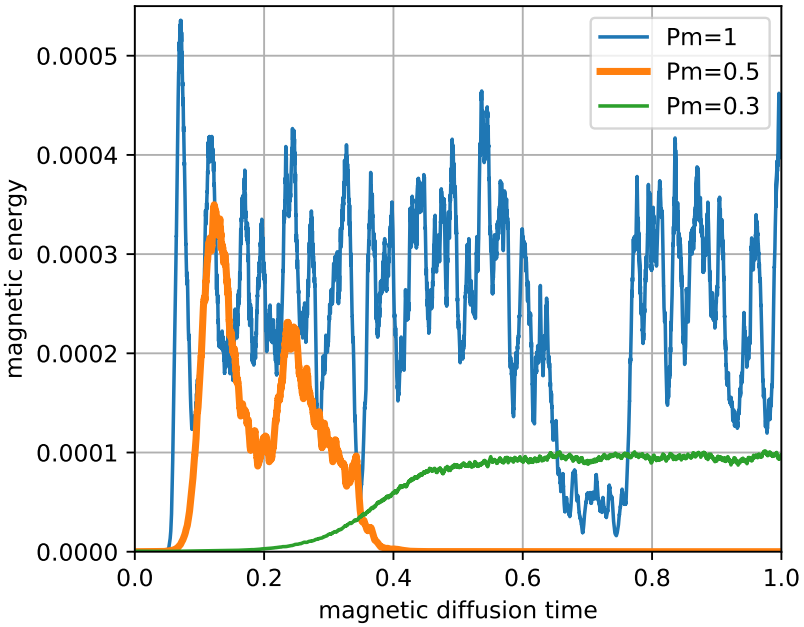

Figure 16: Time-evolution of the magnetic energy in dynamos at $E = 7.94 \times 10^{-5}$, $Po = 0.02$ and $\alpha = 90°$, with a small insulating inner-core $\eta = 0.1$. While $Pm = 0.3$ is a stationary dynamo, the stronger Lorentz force at $Pm = 0.5$ leads to the loss of the magnetic field. One magnetic diffusion time is $R^2(1-\eta)^2\mu\gamma$. The link with large-scale cyclones is shown in supplementary animations `https://doi.org/10.6084/m9.figshare.7063652`.

4.3 Low viscosity dynamos and large-scale vortices

4.3.1 Stable dynamos

Decreasing Po and E together, we find a few stable dynamos in full spheres and spherical shells with a small inner-core ($\eta = 0.1$). The dynamos obtained at the lowest viscosities and forcing (low Pm, E, Po) are all associated with large-scale vortices (LSV, see figure 10 and 19 for examples). The importance of LSV for dynamo action has been already highlighted by Lin et al. (2016), and our study confirms that they play an important role for dynamo action (see also Guervilly et al., 2015, in the context of rotating convection). With stable, persistent LSV, the magnetic energy is rather stable (case $Pm = 0.3$ in figure 16), allowing to obtain dynamos at low viscosity ($Pm < 1$, $E \leq 10^{-4}$), seemingly relevant for planetary cores.

As an example, at $E = 7.94 \times 10^{-5}$, $Po = 0.02$, $\alpha = 90°$, we found a stable saturated dynamo at $Pm = 0.3$ (see figure 16). Three stable LSV are seen during the whole simulation, unaffected by the Lorentz force. Furthermore, the fluid rotation vector does not change significantly from the corresponding hydrodynamic case.

4.3.2 Self-killing dynamos

However, when increasing the electrical conductivity to $Pm = 0.5$, after the exponential growth of the magnetic field, the Lorentz force becomes strong enough to alter the flow so that the magnetic field decays and never recovers, even after the magnetic field has decayed to very low intensity (case $Pm = 0.5$ in figure 16). While the three LSV are present in the growing phase, they wither away when the magnetic field reaches saturation value.

We found other self-killing precessing dynamos as indicated by the triangles in figure 12. At $E = 10^{-5}$, $Po = 0.005$, $\alpha = 90°$, $\eta = 0$, large-scale vortices are observed together with a growing magnetic field for $0.2 \leq Pm \leq 1$ until the Lorentz force kills the vortices and the magnetic field immediately decays. This is illustrated in figure 17a. For the limited time we could run these self-killing dynamos, the LSV and hence also the magnetic field have not been able to recover, event though the field has reached levels where the Lorentz force is negligible. Figure 17b shows that the mean rotation axis of the fluid changes slightly but permanently when the magnetic field reaches its peak intensity. We hypothesize that the slight change in rotational state of the fluid is enough to prevent the reformation of the LSV. Furthermore, the system stays around the second rotational state even though the magnetic field has vanished, which suggests a hydrodynamic bistability.

Self-killing dynamos have already been reported in simple laminar dynamo models (Fuchs et al., 1999) or turbulent experiments (Miralles et al., 2015). To our knowledge, it is the first time such self-killing dynamos are reported in a self-consistent, turbulent setup. Hence, it highlights that kinematic precession dynamos (a growing magnetic field without the Lorentz force) do not imply that strong magnetic fields can be sustained once the Lorentz force is taken into account.

4.3.3 Intermittent dynamos

In addition, many other dynamos show large fluctuations of their magnetic energy of about a factor 10 to 100, suggesting that the Lorentz force is often pushing the flow to a different attractor before quickly recovering. When the magnetic energy is low, the LSV develop and the magnetic field can grow. When the magnetic energy saturates at a high enough level, the Lorentz force sometimes kills the LSV and thus the magnetic energy

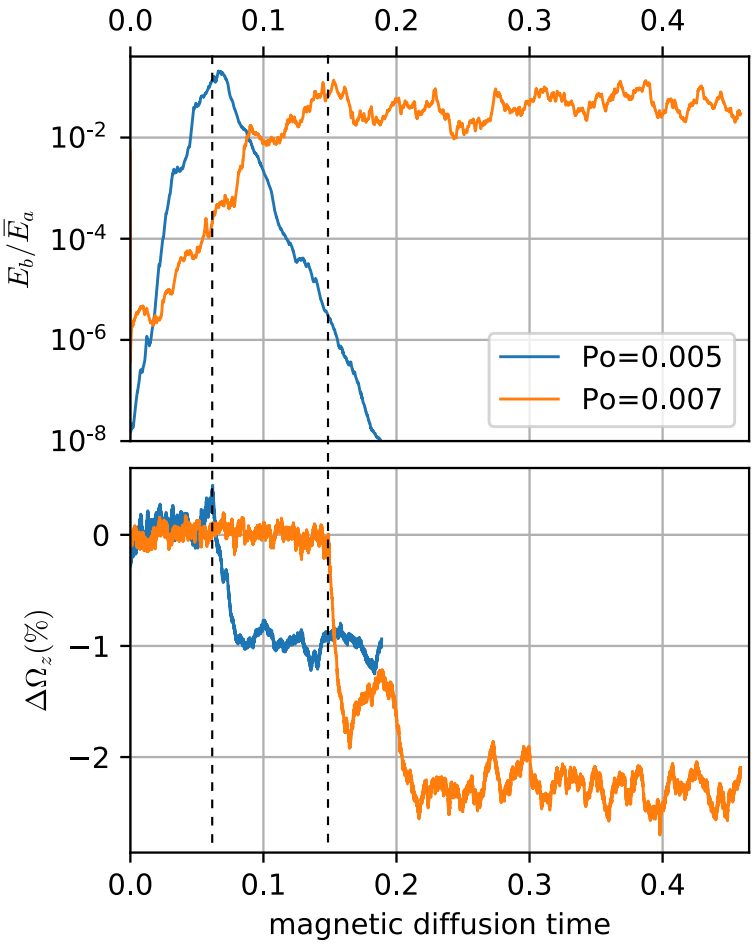

Figure 17: Top: ratio of magnetic energy E_b over time-averaged antisymmetric kinetic energy $\bar{E}_a$. Bottom: relative variations (in percent) of the projection of the fluid rotation axis on the planet spin axis. Both cases have $E = 10^{-5}$, $\alpha = 90°$, $Pm = 0.3$ and no solid inner-core. They differ only by their precession rate Po. The saturation of the magnetic energy at $E_b \approx 0.1\bar{E}_a$ leads to a change in the rotation axis of the fluid, as hinted by the vertical dashed lines. In the case $Po = 0.005$, this change seems permanent despite the loss of the magnetic field. The link with large-scale cyclones is shown in supplementary animations `https://doi.org/10.6084/m9.figshare.7063652`.

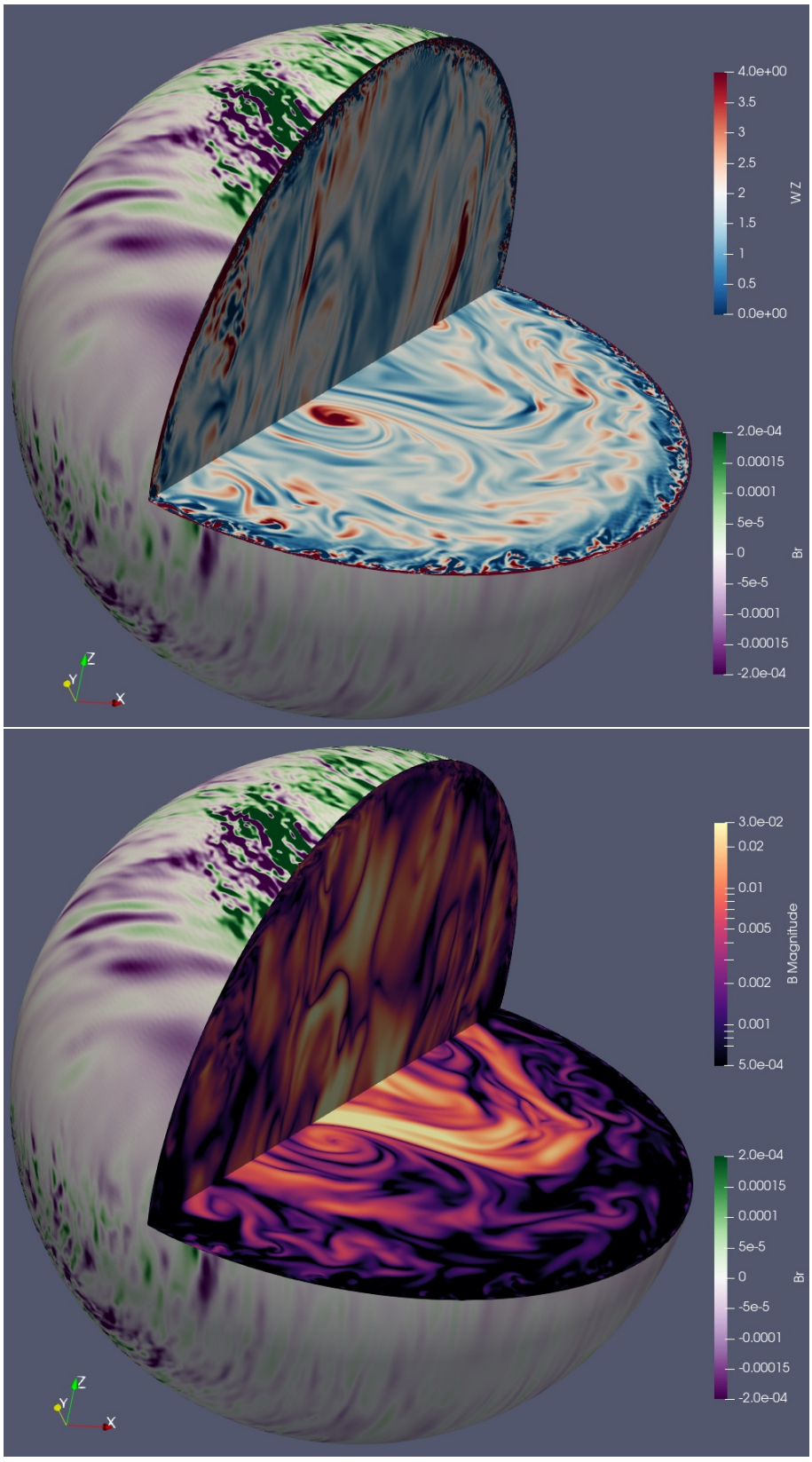

Figure 18: Snapshots (corotating with the fluid) at $E = 10^{-5}$, $Pm = 0.3$, $Po = 0.007$, $\alpha = 90°$ and no solid inner-core. The radial magnetic field is shown on the surface. In the bulk: the axial vorticity along fluid rotation axis (top) and the magnetic intensity (bottom – in logarithmic scale).

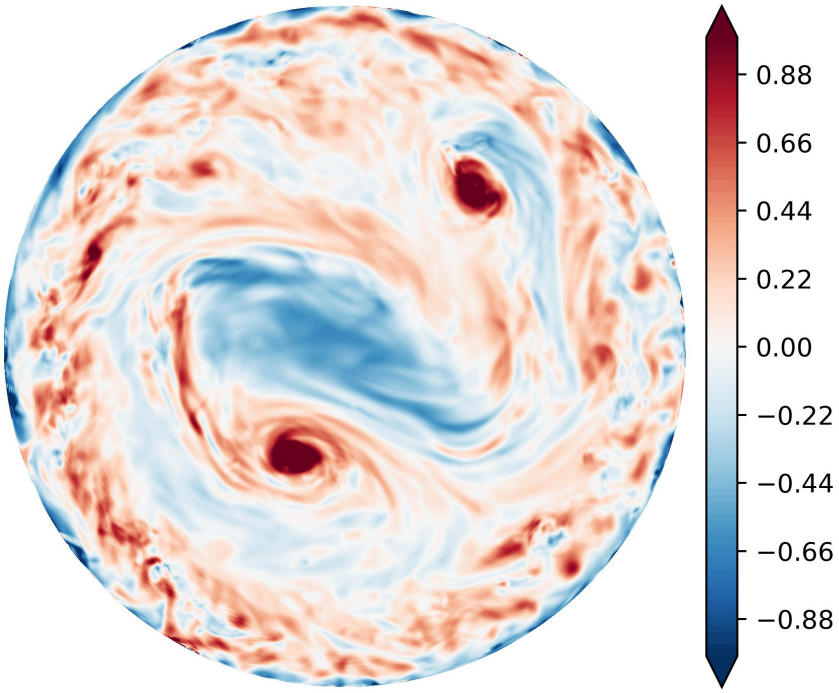

Figure 19: Vorticity along the fluid rotation axis in the frame rotating with the fluid, averaged along the fluid rotation axis, for $E = 10^{-5}$, $Po = 0.007$, $\alpha = 90°$, $Pm = 0.3$. Turbulent boundary layers have been excluded from the average. Two intense cyclones (red) can be seen around a large central anti-cyclonic (blue) region.

decays to a lower level. This behavior is rather common and illustrated by case $Pm = 1$ in figure 16, and case $Po = 0.007$ in figure 17. At the planet's surface, this may appear as an intermittent dynamo, with stronger magnetic field alternating with undetectable magnetic field.

4.3.4 Small-scale surface magnetic field at low viscosity

Keeping $E = 10^{-5}$, $\alpha = 90°$, $\eta = 0$ and increasing the precession rate from $Po = 0.005$ – a self-killing dynamo – to $Po = 0.007$, the LSV are now able to withstand the Lorentz force, and at $Pm = 0.3$ the dynamo saturates with the magnetic energy fluctuating within a factor 10. This is the stable dynamo we obtained with parameters closest to planetary values. Time-evolution of the magnetic energy are shown in figure 17a. A snapshot of the corresponding flow and field is shown in figure 18, while the LSV are highlighted in figure 19. Two large-scale cyclones are seen in the bulk, together with small-scale vorticity fluctuations. Near the outer shell, a thick layer, much thicker than the Ekman layer, of intense small-scale vorticity is seen. This leads to a small-scale magnetic field at the surface, while the larger-scale, stronger field does not escape the bulk. This shift towards small-scale surface magnetic field seems robust as the viscosity is decreased toward planetary values.

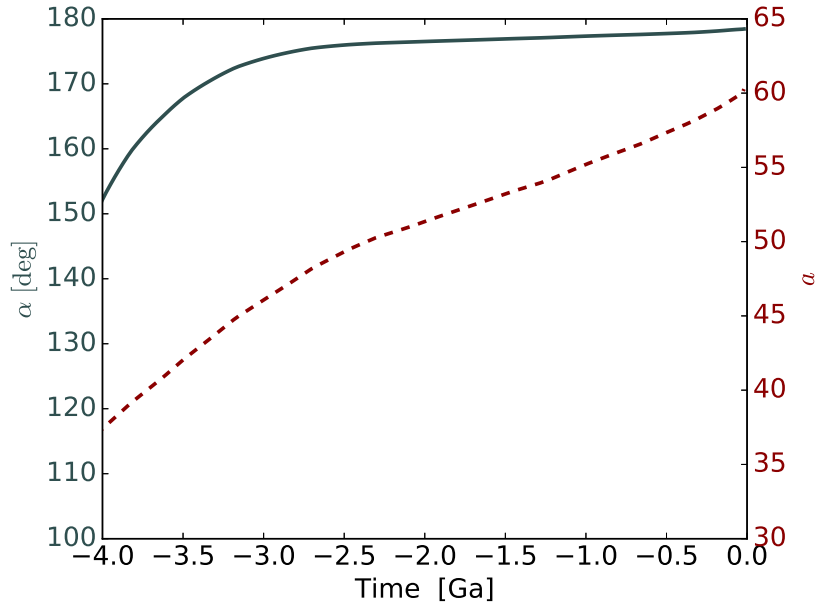

(a)

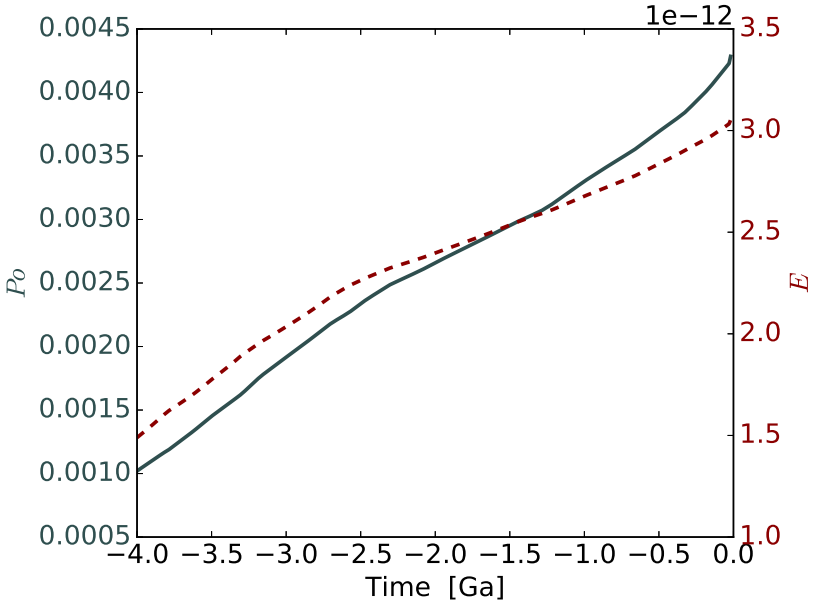

(b)

Figure 20: Time evolution of lunar values. (a) α (solid line), a (dashed line). Note that Dwyer et al. (2011) consider negative values of Po with $\alpha \in [0, 90°]$ whereas, here, our convention is to consider positive Po and $\alpha > 90°$ for retrograde precession. (b) Po (solid line) and E (dashed line), where E is calculated for the liquid core (with $R = 350\,\mathrm{km}$, $\nu = 10^{-6}\,\mathrm{m}^2.\mathrm{s}^{-1}$).

5 Application to the Moon

5.1 Time evolution of the lunar precession

We aim at applying the results obtained above to the time evolution of the Moon. Indeed, precession has been suggested for driving turbulence and dynamo magnetic field in the past Moon liquid core (Dwyer et al., 2011). In the following, we will consider a lunar metallic liquid core, of typical radius $R = 350\,\mathrm{km}$.

The lunar precession angle α is related to the semi-major axis a of the lunar orbit by equation (5) of Dwyer et al. (2011). Then, a is related to time using the so-called nominal model of Dwyer et al. (2011), shown in their figure S2, and reproduced in Fig 20(a).

To calculate Po, we need the lunar precession rate Ω_p, obtained from the Fig. 19 of Touma and Wisdom (1994), and the lunar spin rate Ω_s, given by the orbital rate (synchronized state). Based on the Kepler law $\Omega_s \propto a^{-3/2}$, we thus calculate the evolution of Ω_s from its current value. The time evolution of Po and E over the lunar history are presented in Fig. 20(b).

5.2 Flow stability at the lunar CMB during its history

One can calculate the stability of the lunar liquid core for the parametric instability (CSI-CMB) and the boundary layer instability (BL-CMB). To do so, we define a general parameter ζ as an estimate for the onset distance, given by $\zeta = \epsilon/(K_{CMB}E^{3/10})$ for the CSI-CMB and $\zeta = \epsilon/(K_{BL}E^{1/2})$ for the BL-CMB. An instability is thus expected in both cases when $\zeta > 1$. The results are shown in Fig. 21. It confirms the fact that a CSI-CMB can be currently expected in the Moon, as already proposed by Lin et al. (2015). Beyond this confirmation, this figure furthermore shows that both instabilities are clearly expected during the whole lunar history, with a BL-CMB significantly more unstable.

5.3 Turbulent torque and dissipation in the lunar liquid core

According to Fig. 21, the local Reynolds number $Re = \epsilon/E^{1/2}$ at the lunar CMB has decreased during the lunar evolution, from $Re = 4.10^5$, 4 Ga ago, to its current value of $Re = 10^4$. These values are well in the regime, in which Sous et al. (2013) observe turbulent Ekman layers. A turbulent friction can thus be expected at the lunar CMB, as previously suggested for the current lunar core (Williams et al., 2001). Naturally, a different friction would lead to a different ϵ, and we should thus calculate ϵ in a self-consistent way in presence of a modified friction. To do so, we simply replace the viscous (laminar) term $\mathcal{L}\mathbf{\Gamma}_\nu$ in equations (37)-(39) by the following turbulent damping term:

$$\mathcal{L}\mathbf{\Gamma}_\nu = \lambda_t \, ||\mathbf{\Omega} - \tilde{\mathbf{\Omega}}_{\boldsymbol{s}}|| \, (\mathbf{\Omega} - \tilde{\mathbf{\Omega}}_{\boldsymbol{s}}), \tag{26}$$

with a coefficient λ_t. The dimensionless dissipation can thus generally be written as

$$D_\nu = -I_c \, \lambda_t \, \epsilon^3, \tag{27}$$

where λ_t remains to be obtained. Obtaining expressions of λ_t require to describe the (local) turbulent stress associated to the shear velocity $\boldsymbol{v_{sh}} = (\mathbf{\Omega} - \tilde{\mathbf{\Omega}}_{\boldsymbol{s}}) \times \boldsymbol{r}$ generated by the differential rotation at the inner and outer boundaries. Noting $\boldsymbol{\tau_v}$ the (local) surface stress per unit of mass, one can write $\boldsymbol{\tau_v} = -\kappa |\boldsymbol{v_{sh}}| \boldsymbol{v_{sh}}$, where κ can be seen as a (local)

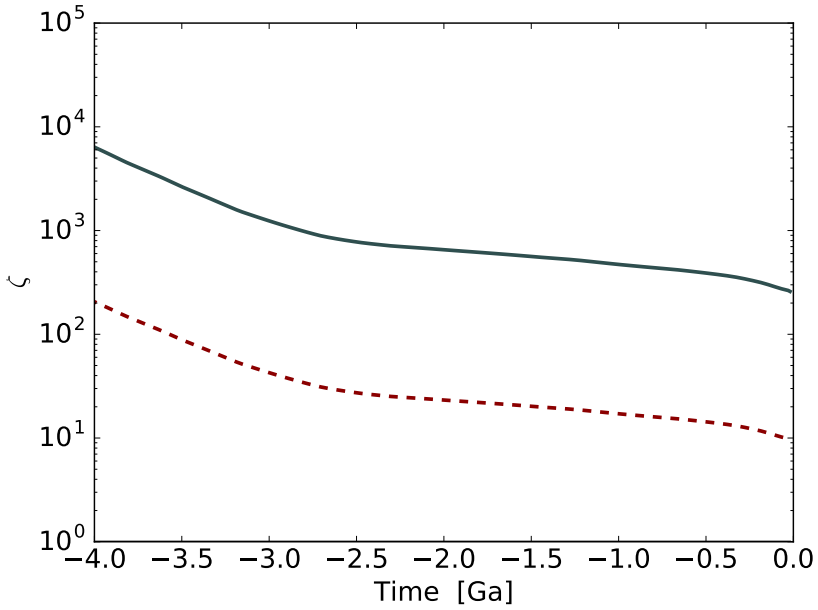

Figure 21: Stability of the lunar liquid core considering the BL-CMB (solid line), with $K_{BL} = 60$, and the CSI-CMB (dashed line), with $K_{CMB} = 8$. Each instability is expected for $\zeta > 1$.

drag coefficient. To close the equations, we need to specify κ, where the physics of the coupling is hidden.

Focusing first on laminar flows, the model of Sous et al. (2013) predicts such flows for $Re \lesssim 150$ and prescribes $\kappa = \xi\epsilon\sqrt{E}/v_{sh}$, where ξ is a constant of order unity ($\xi = 1$ in Sous et al. (2013)). One can then calculate the associated viscous torque $\mathbf{\Gamma}_\nu = \int_S \boldsymbol{r} \times \boldsymbol{\tau_v} \mathrm{d}S$ on the surface S of the fluid boundary. Noting the colatitude θ, we have $|\boldsymbol{r} \times \boldsymbol{\tau_v}| \propto r^3 \sin^3\theta$, which gives

$$\lambda_t = -5\,\xi\,\frac{1+\eta^4\vartheta}{1-\eta^5}\,\frac{E^{1/2}}{\epsilon}, \tag{28}$$

with $\vartheta = 1$ (resp. $\vartheta = 0$) for a no-slip (resp. stress-free) inner boundary. For $Ek \ll 1$ and no-slip boundaries, equation (21) is exactly recovered with $\xi = 2.62/5 \approx 0.52$, including the correct dependency in η (see equation 8). Using this value of ξ allows thus to switch naturally, in the model of Sous et al. (2013), from the validated laminar dissipation (21) to a turbulent dissipation.

In the turbulent regime, it is usually assumed that κ does not vary in space. Under this hypothesis, one can calculate the associated viscous torque $\mathbf{\Gamma}_\nu$ and equation (28) is then modified into

$$\mathbf{\Gamma}_\nu = -\frac{3\pi^2}{4}(1+\eta^5)\kappa|\boldsymbol{v_{sh}}|\boldsymbol{v_{sh}}. \tag{29}$$

Equation (29) recovers equation (55) of Williams et al. (2001) for the particular case $\eta = 0$. Using equation (26), we thus obtain

$$\lambda_t = -\frac{45\pi}{32}\,\frac{1+\eta^5\vartheta}{1-\eta^5}\,\kappa, \tag{30}$$

with ϑ defined as above. Note the different dependency in η compared to equation (28).

To close the equations in the turbulent regime, a value has to be chosen for κ (assumed to be uniform in space). As a first approach, Yoder (1981) simply considered a constant $\kappa = 0.002$ based on Bowden (1953). Later, refined models based on turbulent boundary layer theory have been proposed (Yoder, 1995; Williams et al., 2001). However, in these models, rotation effects are not included in the turbulent boundary layer theory, and ϵ has to be calculated self-consistently, i.e. by taking into account the interdependency of ϵ and λ_t . Here, we propose to solve this issue by self-consistently calculating ϵ and λ_t via the torque balance (37)-(39), and the formulas of Sous et al. (2013). Following Sous et al. (2013), we thus use $\kappa = C_d \cos\alpha_0$ for turbulent flows ($Re > 150$), where

$$C_d = \frac{u_{0\star}^2}{\epsilon^2} = \frac{k^2}{\left(\ln\left|\frac{u_{0\star}}{2z_0}\right| - A\right)^2 + B^2}. \tag{31}$$

In equation (31), $u_{0\star}$ is an unknown, $k = 0.4$ is the von Karman constant, (A, B) are constants, and $\sin\alpha_0 = (Bu_{0\star})/(k\epsilon)$. From atmospheric measurements, we typically have $(A, B) = (1.3, 4.4)$, whereas laboratory experiments rather give $(A, B) = (3.3, 3)$ (Sous et al., 2013). Noting z_r the dimensionless root mean square roughness height of the boundary, $z_0 = 0.11E/u_{0\star}$ for a smooth CMB (i.e. $z_r u_{0\star}/E < 60$), whereas $z_0 = z_r/30$ for a rough CMB (i.e. $z_r u_{0\star}/E > 60$). We deduce λ_t from equation (31). Considering a smooth boundary, equation (58b) of Williams et al. (2001), where the rotation is not taken into account, is recovered with $B = 0$ and $z_0/E = 1.25\,\mathrm{e}^{-A}/\epsilon$, to compare with the equation $z_0/E = 0.11/u_{0\star}$ of Sous et al. (2013). We implemented this self-consistent turbulent friction in the updated FLIPPER program, which can be found at `https://www.mathworks.com/matlabcentral/fileexchange/50612-flipper`.

In Fig.22, one can clearly see that the model based on Sous et al. (2013) recovers well the laminar dissipation $D_\nu \propto I_c \epsilon^2 \sqrt{E}$, for large enough E, and the turbulent dissipation $D_\nu \propto I_c \epsilon^3$ advocated by (Yoder, 1981) for $E \ll 1$ (with similar values). However, this model also describes the transition between these two limit models and improve the turbulent model by taking the boundary roughness into account. Note in particular the difference of behaviours, for $E \ll 1$ between the smooth and the rough boundary cases.

Taking into account a polar flattening of $2.5 \cdot 10^{-5}$ for the lunar core, we solve the torque balance (37)-(39) using the lunar parameters. The results are shown in Fig.23 for the different models of viscous torques discussed above. Recovering that a laminar dissipation is not consistent with the currently observed dissipation (Williams et al., 2001), we also show here that the dissipation is expected to be turbulent during the whole lunar history. We also show here the the simple model of Yoder (1981) gives quite good estimates. Note finally that, taking an inner core into account, even with $\eta = 0.7$ (Weber et al., 2011), does not strongly modify the dissipation (modification by a factor smaller than 56% for a smooth CMB).

6 Conclusion

In this study, we have characterized the precession driven instabilities necessary to sustain magnetic fields in planetary cores. At larger viscosities, the boundary layers remain stable, while parametric resonances (CSI) lead to bulk instabilities. At lower viscosities, the Ekman boundary layer becomes highly turbulent while the CSI is still stirring the bulk. Varying the inner-core size, we characterize both the evolution of the onset and the

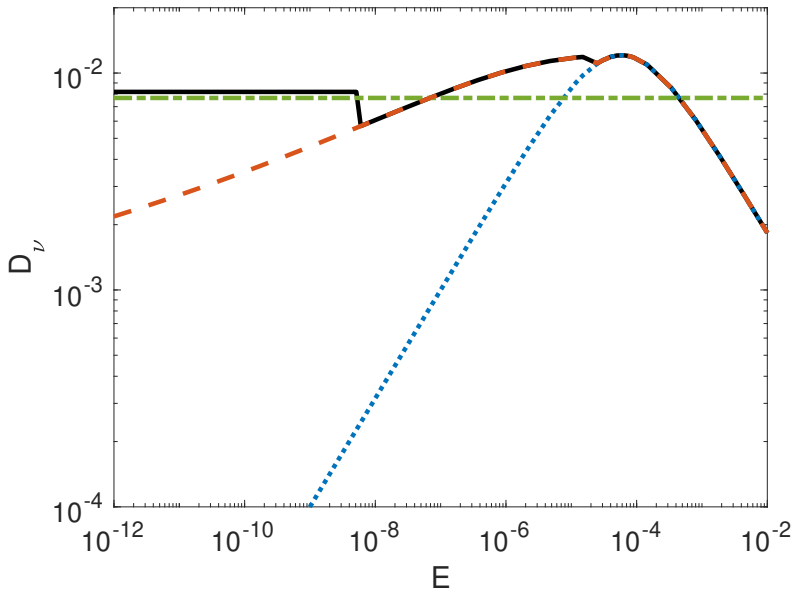

Figure 22: (a) Dissipation of the model based on Sous et al. (2013) for a smooth (dashed line) and a rough CMB (solid line) with $z_r = 10^{-5}$, of the mode (horizontal dash-dotted line) of Yoder (1981), and, as a dotted line, of the laminar reduced model (21) using equation (9), $\lambda_r = -2.62$, $\lambda_i = 0$. Parameters: $Po = 0.02$, $\alpha = \pi/3$, $\eta = 0$, $(A, B) = (3.3, 3)$, $\xi = 0.52$.

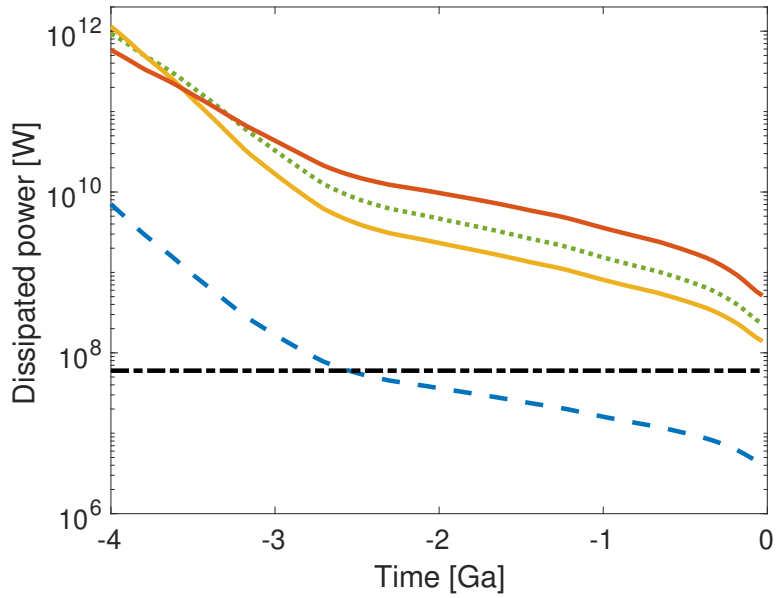

Figure 23: Dissipated power in the lunar core given by models, compared to the current dissipation (horizontal dash-dotted line) of 6.10^7 W, derived from the Lunar Laser Ranging (LLR) data (Williams et al., 2001). Laminar model as a dashed line, model of Yoder (1981) as a dotted line, and the model of Sous et al. (2013) as solid lines (smooth CMB and $z_r = 10^{-5}$ for the lowermost and the uppermost ones at -1 Ga).

dissipation with the shell aspect ratio η. We find that it influences only weakly the onset, which is compatible with experimental findings in a librating ellipsoid (Lemasquerier et al., 2017). While our simulations are still dominated by laminar dissipation, we expect the dissipation in planetary cores to be governed by turbulence in the boundary layers. Based on our numerical results and the experimental work of Sous et al. (2013), we have derived a self-consistent model of the dissipation in precession spherical shells, including both turbulent friction, inner-core and rotation effects. Extrapolating our model to the lunar core, we predict dissipation compatible with the observed LLR data, with little sensitivity to the size of an inner-core.

Adding the magnetic field, we examine the dynamo action over a wide range of parameters towards the planetary regime ($E, Pm, Po \ll 1$). At the lowest investigated viscosity $E = 10^{-5}$ we found a self-sustained magnetic field at $Pm = 0.3$ and $Po = 0.007$. Besides the laminar dynamos at high viscosity which are not relevant for planets, three types of dynamo behaviours emerge at low viscosity ($Pm < 1$, $E \leq 10^{-4}$): (i) stable dynamos, where the magnetic energy reaches a statistically steady state with low to moderate fluctuations; (ii) intermittent dynamos, where the system oscillates between two states with different mean magnetic energies corresponding to two slightly different directions of the fluid rotation axis; (iii) self-killing dynamos, where the magnetic field grows exponentially, saturates but finally decays. At low viscosity, two or three large-scale cyclonic vortices (LSV) are observed during the initial exponential growth of the magnetic field in all three cases. We suspect that far from their onset, LSV can withstand the Lorentz force leading to stable dynamos. Furthermore, in the regime of $Po < 0.1$, stable dynamos without LSV have been seen only with $Pm \geq 1$. Our results suggest that LSV play a key role in magnetic field generation in (spherical) planetary cores.

Despite the large number of simulations, predictive scaling laws remain elusive for the kinetic energy stored in the instabilities, for the onset of dynamo action, and for the magnetic field strength. These quantities have a non-monotonic behaviour when varying the key control parameters E and Po, and an asymptotic regime has yet to be reached. Goepfert and Tilgner (2018) also draw similar conclusions for dynamos in a precessing cube. This suggests that the non-monotonic behaviour is not linked to the spherical shape, but rather to the precession itself. For $Pm \leq 2$, the magnetic energy seems capped by the turbulent kinetic energy, in contrast to convective dynamos where magnetic energy overcomes kinetic energy as viscosity is lowered (e.g. Schaeffer et al., 2017). Predicting the turbulent kinetic energy is an outstanding issue, as only a few of our simulations reach the regime where departures from laminar dissipation is expected. Exploring this challenging regime relevant for planetary cores is however a necessary first step towards extracting useful scaling laws – if such laws exist for this system. We release our simulation database to enable further investigations and contributions.

None of our dynamos produce a predominantly dipolar field. Furthermore, at small Ekman number, while the magnetic field is generated in the bulk at the large scale of the LSV, the surface magnetic field is more and more dominated by small scales. This shift towards small-scale surface fields as the viscosity is lowered was observed for other spherical dynamos driven by the boundaries (Monteux et al., 2012). Indeed, intense small-scale turbulence develops in the boundary layers, shredding the magnetic field to small scales. This contrasts with convective dynamos for which a wide range of parameters lead to dipolar fields (e.g. Kutzner and Christensen, 2002).

For a precessing spheroid, a topography driven instability may occur (Vidal and Cébron, 2017) while the boundary layers remain stable. In this case, no small-scale

turbulence would shred the magnetic field in the boundary layer, permitting a surface field on the same scale as in the bulk.

Acknowledgments

We thank Yufeng Lin for sharing his data with us. Numerical simulations were performed using the XSHELLS code which is freely available at `https://bitbucket.org/nschaeff/xshells`. Our dataset built from our simulations is available at `https://doi.org/10.6084/m9.figshare.7063652`.

This work was performed using HPC resource Occigen from CINES under allocations x2016047382, A0020407382 and A0040407382 made by GENCI. Part of the computations were also performed on the Froggy platform of CIMENT (`https://ciment.ujf-grenoble.fr`), supported by the Rhône-Alpes region (CPER07_13 CIRA), OSUG@2020 LabEx (ANR10 LABX56) and Equip@Meso (ANR10 EQPX-29-01). NS and DC were supported by the French *Agence Nationale de la Recherche* under grant ANR-14-CE33-0012 (MagLune). ISTerre is part of Labex OSUG@2020 (ANR10 LABX56). RL would like to acknowledge support from the European Research Council (ERC Advanced grant 670874 ROTANUT) and the HPC resources of the Royal Observatory of Belgium.

A Theoretical solutions for the forced base flow

In this appendix, we consider the usual planetary relevant limit $Po \ll 1$ considered in the literature. In this limit, the unit of time Ω_o^{-1} corresponds to the usual unit of time Ω_s^{-1}.

A.1 The model of Busse (1968)

The equations governing the steady uniform vorticity bulk component of the flow can be written as (e.g. Noir et al. (2003); Cébron et al. (2010))

$$\Omega_z = \Omega_x^2 + \Omega_y^2 + \Omega_z^2, \tag{32}$$

$$-P_z\ \Omega_y = (\lambda_r\ \Omega_x \Omega_z^{1/4} + \lambda_i\ \Omega_y \Omega_z^{-1/4})\sqrt{E}, \tag{33}$$

$$P_x\ \Omega_y = -\lambda_r\ \Omega_z^{1/4}\ (1-\Omega_z)\ \sqrt{E}, \tag{34}$$

which are exactly the equations (20)-(22) of Noir et al. (2003), or the equations (21)-(23) of Cébron et al. (2010) in the particular case of a sphere (no deformation, and $P_y = 0$ in their equations). As shown by Noir et al. (2003), this system of equations is equivalent to the well-known implicit expression (3.19) of Busse (1968). Equation (32) is the so-called no spin-up condition (solvability condition 3.14 of Busse (1968), or equation (12) of Noir et al. (2003)) given that it forbids any differential rotation along $\mathbf{\Omega}$. Equations (33)-(34) are simply obtained from a torque balance (see Noir et al. (2003); Cébron et al. (2010) for details).

In equations (32)-(34), we have noted the spin-over damping factor $\underline{\lambda} = \lambda_r + \mathrm{i}\lambda_i$, given by

$$\underline{\lambda}_{inv}^{sphere} = -\frac{3[19(1-\mathrm{i}) + 9\sqrt{3}(1+\mathrm{i})]}{28\sqrt{2}} \approx -2.62 + 0.258\mathrm{i} \tag{35}$$

for a spherical container ($\eta = 0$), in the inviscid limit $E \ll 1$. For finite values of E, Noir et al. (2001) has obtained empirically $\lambda_r \approx -2.62 - 1.36E^{0.27}$, and a fit of the results of Hollerbach and Kerswell (1995) gives $\lambda_i \approx 0.258 + 1.25E^{0.21}$.

Even if equations (32)-(34) are obtained without any inner core, corrections have been proposed for the case of the sphere to take a spherical inner core into account. Using the dimensionless inner radius r_i, it has been proposed to simply modify $\underline{\lambda}$ by the factor $(1+\eta^4)/(1-\eta^5)$ for a no-slip inner core Hollerbach and Kerswell (1995), and by $1/(1-\eta^5)$ for a stress-free inner core Tilgner and Busse (2001). Using the results of Hollerbach and Kerswell (1995) for the spherical shell, the corrections for viscous and aspect ratio effects can be combined following

$$\underline{\lambda} \approx \left[\underline{\lambda}_{inv}^{sphere} - 1.36E^{0.27} + \mathrm{i}\,1.25E^{0.21}\right] \frac{1+\eta^4}{1-\eta^5}, \tag{36}$$

with $\underline{\lambda} = \lambda_r + \mathrm{i}\lambda_i$.

A.2 Approximate explicit solution

As shown by Noir and Cébron (2013), (32)-(34) can be obtained as fixed points of a dynamical model for $\mathbf{\Omega}$, given by (see equations A14-A 16 of Noir and Cébron (2013) for a spheroid)

$$\frac{\partial \Omega_x}{\partial t} = P_z\Omega_y - (1-\gamma)\left[P_z\Omega_y + \Omega_y\Omega_z\right] + \mathcal{L}\mathbf{\Gamma}_\nu \cdot \hat{\boldsymbol{x}}, \tag{37}$$

$$\frac{\partial \Omega_y}{\partial t} = P_x\Omega_z - P_z\Omega_x + (1-\gamma)\left[P_z\Omega_x + \Omega_x\Omega_z\right] + \mathcal{L}\mathbf{\Gamma}_\nu \cdot \hat{\boldsymbol{y}}, \tag{38}$$

$$\frac{\partial \Omega_z}{\partial t} = -P_x\Omega_y - (1-\gamma)P_x\Omega_y + \mathcal{L}\mathbf{\Gamma}_\nu \cdot \hat{\boldsymbol{z}}, \tag{39}$$

where $\gamma = (2a^2)/(a^2+c^2)$ represents the ratio of the polar to equatorial moment of inertia, where $\mathbf{\Gamma}_\nu$ is the viscous torque, and where $\mathcal{L}$ is a 3x3 matrix given by equation (A3) of Noir and Cébron (2013). For the sphere, $\mathcal{L}$ reduces to $\mathcal{L} = 15\delta_{ij}/(8\pi(1-\eta^5))$, using the Kronecker delta δ_{ij}. As detailed by Cébron (2015), equations (32)-(34) are then recovered with

$$\mathcal{L}\mathbf{\Gamma}_\nu = \sqrt{\Omega E}\left[\lambda_r \begin{pmatrix} \Omega_x \\ \Omega_y \\ \Omega_z - 1 \end{pmatrix} + \frac{\lambda_i}{\Omega}\begin{pmatrix} \Omega_y \\ -\Omega_x \\ 0 \end{pmatrix}\right]. \tag{40}$$

To obtain tractable analytical solutions, we need a simpler set of equations. We thus follow Noir and Cébron (2013) who linearize $\mathcal{L}\mathbf{\Gamma}_\nu$ by assuming that the fluid rotates at the same rate than the boundaries, i.e. $\Omega = 1$, which gives

$$\mathcal{L}\mathbf{\Gamma}_\nu = \sqrt{E}\left[\lambda_r \begin{pmatrix} \Omega_x \\ \Omega_y \\ \Omega_z - 1 \end{pmatrix} + \lambda_i \begin{pmatrix} \Omega_y \\ -\Omega_x \\ 0 \end{pmatrix}\right]. \tag{41}$$

Focusing on stationary solutions of equations (37)-(39) with the viscous term (41), the explicit solution for $\mathbf{\Omega}$ is then

$$\Omega_x = \frac{\left[\lambda_i + \chi\cos\alpha\right]\chi\sin\alpha}{\chi(\chi + 2\lambda_i\cos\alpha) + |\underline{\lambda}|^2}, \tag{42}$$

$$\Omega_y = -\frac{\chi\lambda_r\sin(\alpha)}{\chi(\chi + 2\lambda_i\cos\alpha) + |\underline{\lambda}|^2}, \tag{43}$$

$$\Omega_z = \frac{\chi(\chi\cos^2\alpha + 2\lambda_i\cos\alpha) + |\underline{\lambda}|^2}{\chi(\chi + 2\lambda_i\cos\alpha) + |\underline{\lambda}|^2}, \tag{44}$$

where $\chi = Po/\sqrt{E}$, and $|\underline{\lambda}|^2 = \lambda_r^2 + \lambda_i^2$. The differential rotation ϵ of the fluid with the boundary is thus:

$$\epsilon = \frac{|\chi \sin\alpha|}{\sqrt{\chi(\chi + 2\lambda_i \cos\alpha) + |\underline{\lambda}|^2}}. \tag{45}$$

Note that these explicit expressions for $\mathbf{\Omega}$ allows to precise quantitatively various observations, previously noticed in the literature. For instance, Noir and Cébron (2013) have considered the resonance of ϵ for a fixed Rossby number $Ro = Po \sin\alpha$, i.e. the value of Po where ϵ is maximum when Ro is maintained constant. They have noticed that the role of λ_i is mainly to shift the resonance peak, that the reduced model (41) always gives at $Po = 0$ for the sphere when $\lambda_i = 0$ is assumed. We can thus use expressions (42)-45 to precise this observation. For a given Ro, we obtain that the resonance is indeed reached for $Po = 0$ when $\lambda_i = 0$, but the resonance is shifted to

$$\chi = Po/\sqrt{E} = -\lambda_i \sqrt{1 + Ro^2/\lambda_i^2} \tag{46}$$

when $\lambda_i \neq 0$. It is straightforward to show that, at the resonance, Ω_x is zero whereas Ω_y and Ω_z are respectively maximum and minimum.

One can finally notice that the additional hypothesis $\lambda_i = 0$, considered e.g. by Noir and Cébron (2013) and Cébron (2015), allows to simplify equations (42)-(44) into

$$\Omega = \left(\frac{1}{2} \frac{\sin 2\alpha}{1+x^2}, -\frac{x \sin\alpha}{1+x^2}, \frac{x^2 + \cos^2\alpha}{1+x^2} \right), \tag{47}$$

which gives

$$\epsilon = \frac{|\sin\alpha|}{\sqrt{1+x^2}}, \tag{48}$$

where $x = \lambda_r/\chi$. Note that Ω_x, Ω_z and ϵ are maximum for $x = 0$, whereas Ω_y is maximum for $x = \pm 1$. It is interesting to note that equation (48) is exactly equation (53) of Williams et al. (2001), but we manage here to obtain an explicit expression for x.

References

Boisson, J., Cébron, D., Moisy, F., and Cortet, P.-P. (2012). Earth rotation prevents exact solid-body rotation of fluids in the laboratory. *EPL (Europhysics Letters)*, 98(5):59002.

Bowden, K. (1953). Note on wind drift in a channel in the presence of tidal currents. *Proc. R. Soc. Lond. A*, 219(1139):426–446.

Busse, F. H. (1968). Steady fluid flow in a precessing spheroidal shell. *Journal of Fluid Mechanics*, 33(04):739–751.

Calkins, M. A., Noir, J., Eldredge, J. D., and Aurnou, J. M. (2010). Axisymmetric simulations of libration-driven fluid dynamics in a spherical shell geometry. *Physics of Fluids*, 22(8):086602.

Cébron, D. (2015). Bistable flows in precessing spheroids. *Fluid Dynamics Research*, 47(2):025504.

Cébron, D. and Hollerbach, R. (2014). Tidally driven dynamos in a rotating sphere. *The Astrophysical Journal Letters*, 789(1):L25.

Cébron, D., Le Bars, M., and Meunier, P. (2010). Tilt-over mode in a precessing triaxial ellipsoid. *Physics of Fluids*, 22(11):116601.

Dwyer, C. A., Stevenson, D. J., and Nimmo, F. (2011). A long-lived lunar dynamo driven by continuous mechanical stirring. *Nature*, 479(7372):212–214.

Faller, A. J. (1991). Instability and transition of disturbed flow over a rotating disk. *Journal of Fluid Mechanics*, 230:245–269.

Fuchs, H., Rädler, K.-H., and Rheinhard, M. (1999). On self–killing and self–creating dynamos. *Astronomische Nachrichten: News in Astronomy and Astrophysics*, 320(3):129–133.

Giesecke, A., Vogt, T., Gundrum, T., and Stefani, F. (2018). Nonlinear large scale flow in a precessing cylinder and its ability to drive dynamo action. *Physical review letters*, 120(2):024502.

Goepfert, O. and Tilgner, A. (2016). Dynamos in precessing cubes. *New Journal of Physics*, 18:103019.

Goepfert, O. and Tilgner, A. (2018). Mechanisms for magnetic field generation in precessing cubes. *Geophysical & Astrophysical Fluid Dynamics*, pages 1–13.

Goto, S., Matsunaga, A., Fujiwara, M., Nishioka, M., Kida, S., Yamato, M., and Tsuda, S. (2014). Turbulence driven by precession in spherical and slightly elongated spheroidal cavities. *Physics of Fluids*, 26(5):055107.

Greenspan, H. P. G. et al. (1968). *The theory of rotating fluids*. CUP Archive.

Guervilly, C., Hughes, D. W., and Jones, C. A. (2015). Generation of magnetic fields by large-scale vortices in rotating convection. *Physical Review E*, 91(4):041001.

Hollerbach, R. and Kerswell, R. (1995). Oscillatory internal shear layers in rotating and precessing flows. *Journal of Fluid Mechanics*, 298:327–339.

Hollerbach, R., Nore, C., Marti, P., Vantieghem, S., Luddens, F., and Léorat, J. (2013). Parity-breaking flows in precessing spherical containers. *Physical Review E*, 87(5):053020.

Hough, S. S. (1895). The oscillations of a rotating ellipsoidal shell containing fluid. *Philosophical Transactions of the Royal Society of London A*, pages 469–506.

Kerswell, R. R. (1995). On the internal shear layers spawned by the critical regions in oscillatory Ekman boundary layers. *Journal of Fluid Mechanics*, 298:311–325.

Kerswell, R. R. (1996). Upper bounds on the energy dissipation in turbulent precession. *Journal of Fluid Mechanics*, 321:335–370.

Kerswell, R. R. (2002). Elliptical instability. *Annual Review of Fluid Mechanics*, 34(1):83–113.

Kida, S. (2011). Steady flow in a rapidly rotating sphere with weak precession. *Journal of Fluid Mechanics*, 680:150–193.

Kida, S. (2018). Steady flow in a rotating sphere with strong precession. *Fluid Dynamics Research*, 50(2):021401.

Kutzner, C. and Christensen, U. (2002). From stable dipolar towards reversing numerical dynamos. *Physics of the Earth and Planetary Interiors*, 131(1):29–45.

Le Bars, M., Cébron, D., and Le Gal, P. (2015). Flows driven by libration, precession, and tides. *Annual Review of Fluid Mechanics*, 47:163–193.

Le Dizès, S. and Le Bars, M. (2017). Internal shear layers from librating objects. *Journal of Fluid Mechanics*, 826:653–675.

Lemasquerier, D., Grannan, A. M., Vidal, J., Cébron, D., Favier, B., Le Bars, M., and Aurnou, J. M. (2017). Libration-driven flows in ellipsoidal shells. *Journal of Geophysical Research: Planets*, 122(9):1926–1950.

Lin, Y., Marti, P., and Noir, J. (2015). Shear-driven parametric instability in a precessing sphere. *Physics of Fluids*, 27(4):046601.

Lin, Y., Marti, P., Noir, J., and Jackson, A. (2016). Precession-driven dynamos in a full sphere and the role of large scale cyclonic vortices. *Physics of Fluids*, 28(6):066601.

Lingwood, R. J. (1997). Absolute instability of the ekman layer and related rotating flows. *Journal of Fluid Mechanics*, 331:405–428.

Lorenzani, S. (2001). *Fluid instabilities in precessing ellipsoidal shells*. PhD thesis, Niedersächsische Staats-und Universitätsbibliothek Göttingen.

Malkus, W. V. R. (1968). Precession of the Earth as the cause of geomagnetism. *Science*, 160(3825):259–264.

Marti, P., Schaeffer, N., Hollerbach, R., Cébron, D., Nore, C., Luddens, F., Guermond, J.-L., Aubert, J., Takehiro, S., Sasaki, Y., Hayashi, Y.-Y., Simitev, R., Busse, F., Vantieghem, S., and Jackson, A. (2014). Full sphere hydrodynamic and dynamo benchmarks. *Geophysical Journal International*, 197(1):119–134.

Matsui, H., Heien, E., Aubert, J., Aurnou, J. M., Avery, M., Brown, B., Buffett, B. A., Busse, F., Christensen, U. R., Davies, C. J., et al. (2016). Performance benchmarks for a next generation numerical dynamo model. *Geochemistry, Geophysics, Geosystems*, 17(5):1586–1607.

Miralles, S., Plihon, N., and Pinton, J.-F. (2015). Lorentz force effects in the bullard–von kármán dynamo: saturation, energy balance and subcriticality. *Journal of Fluid Mechanics*, 775:501–523.

Monteux, J., Schaeffer, N., Amit, H., and Cardin, P. (2012). Can a sinking metallic diapir generate a dynamo? *Journal of Geophysical Research: Planets*, 117(E10).

Noir, J., Cardin, P., Jault, D., and Masson, J.-P. (2003). Experimental evidence of non-linear resonance effects between retrograde precession and the tilt-over mode within a spheroid. *Geophysical Journal International*, 154(2):407–416.

Noir, J. and Cébron, D. (2013). Precession-driven flows in non-axisymmetric ellipsoids. *Journal of Fluid Mechanics*, 737:412–439.

Noir, J., Jault, D., and Cardin, P. (2001). Numerical study of the motions within a slowly precessing sphere at low Ekman number. *Journal of Fluid Mechanics*, 437:283–299.

Nore, C., Léorat, J., Guermond, J., and Luddens, F. (2011). Nonlinear dynamo action in a precessing cylindrical container. *Physical Review E*, 84(1):016317.

Poincaré, H. (1910). Sur la précession des corps déformables. *Bulletin Astronomique, Serie I*, 27:321–356.

Pozzo, M., Davies, C., Gubbins, D., and Alfe, D. (2012). Thermal and electrical conductivity of iron at Earth's core conditions. *Nature*, 485(7398):355–361.

Rieutord, M. (2001). Ekman layers and the damping of inertial r-modes in a spherical shell: application to neutron stars. *The Astrophysical Journal*, 550(1):443.

Schaeffer, N. (2013). Efficient spherical harmonic transforms aimed at pseudospectral numerical simulations. *Geochemistry, Geophysics, Geosystems*, 14(3):751–758.

Schaeffer, N., Jault, D., Nataf, H.-C., and Fournier, A. (2017). Turbulent geodynamo simulations: a leap towards Earths core. *Geophysical Journal International*, 211(1):1–29.

Sloudsky, T. (1895). De la rotation de la Terre supposée fluide à son intérieur. *Bull. Soc. Imp. Natur. Mosc.*, IX:285–318.

Sous, D., Sommeria, J., and Boyer, D. (2013). Friction law and turbulent properties in a laboratory ekman boundary layer. *Physics of Fluids*, 25(4):046602.

Stegman, D., Jellinek, A., Zatman, S., Baumgardner, J., and Richards, M. (2003). An early lunar core dynamo driven by thermochemical mantle convection. *Nature*, 421(6919):143–146.

Stewartson, K. and Roberts, P. H. (1963). On the motion of liquid in a spheroidal cavity of a precessing rigid body. *Journal of Fluid Mechanics*, 17(01):1–20.

Tilgner, A. (2005). Precession driven dynamos. *Physics of Fluids*, 17(3):034104.

Tilgner, A. (2007). Kinematic dynamos with precession driven flow in a sphere. *Geophysical & Astrophysical Fluid Dynamics*, 101(1):1–9.

Tilgner, A. and Busse, F. H. (2001). Fluid flows in precessing spherical shells. *Journal of Fluid Mechanics*, 426:387–396.

Touma, J. and Wisdom, J. (1994). Evolution of the earth-moon system. *The Astronomical Journal*, 108:1943–1961.

Vidal, J. and Cébron, D. (2017). Inviscid instabilities in rotating ellipsoids on eccentric Kepler orbits. *Journal of Fluid Mechanics*, 833:469–511.

Vidal, J., Cébron, D., Schaeffer, N., and Hollerbach, R. (2018). Magnetic fields driven by tidal mixing in radiative stars. *Monthly Notices of the Royal Astronomical Society*, 475(4):4579–4594.

Vormann, J. and Hansen, U. (2018). Numerical simulations of bistable flows in precessing spheroidal shells. *Geophysical Journal International*, 213(2):786–797.

Weber, R. C., Lin, P.-Y., Garnero, E. J., Williams, Q., and Lognonne, P. (2011). Seismic detection of the lunar core. *science*, 331(6015):309–312.

Williams, J. G., Boggs, D. H., Yoder, C. F., Ratcliff, J. T., and D., J. O. (2001). Lunar rotational dissipation in solid body and molten core. *Journal of Geophysical Research: Planets*, 106(E11):27933–27968.

Wu, C.-C. and Roberts, P. H. (2013). On a dynamo driven topographically by longitudinal libration. *Geophysical & Astrophysical Fluid Dynamics*, 107(1-2):20–44.

Yoder, C. F. (1981). The free librations of a dissipative moon. *Phil. Trans. R. Soc. Lond. A*, 303(1477):327–338.

Yoder, C. F. (1995). Venus' free obliquity. *Icarus*, 117(2):250–286.

Zhang, K., Chan, K. H., and Liao, X. (2010). On fluid flows in precessing spheres in the mantle frame of reference. *Physics of Fluids*, 22(11):116604.